Fast inversion of magnetic field maps of unidirectional planar geological magnetization

Eduardo A. Lima,[1] Benjamin P. Weiss,[1] Laurent Baratchart,[2] Douglas P. Hardin,[3] and Edward B. Saff[3]

[1]   Scanning magnetic microscopes are being increasingly utilized in paleomagnetic studies of geological samples. These instruments typically map a single component of the sample's magnetic field at close proximity with submillimeter horizontal spatial resolution. However, in most applications, an image of the magnetization distribution within the sample is desired rather than its external magnetic field. This requires carefully solving an ill-posed inverse problem to obtain solutions that are nearly free of artifacts and consistent with both natural and laboratory magnetization processes. We present a new, fast inversion technique based on classic methods developed for the Fourier domain that retrieves planar unidirectional magnetization distributions from magnetic field maps. Whereas our approach considers the subtle peculiarities of scanning magnetic microscopy which otherwise can complicate this technique, much of the formalism and algorithms described in this work can also be directly applied to province-scale magnetic field data from aeromagnetic surveys and may be used as an initial step in the modeling of magnetic sources with complex three-dimensional geometries. We discuss sources of inaccuracy observed in practical implementations of the technique and present strategies to improve the quality of inversions. Numerous examples of inversion of both synthetic and experimental data demonstrate the performance of the technique under different conditions. In particular, we retrieve magnetization distributions of a Hawaiian basalt and compare it to inversions calculated in a previous work. We conclude by showing a reconstructed magnetization for the eucrite meteorite ALHA81001 that displays in high resolution the spatial distribution of high-coercivity grains within the sample.

1.   Introduction

[2]   Techniques for imaging magnetization distributions in geological samples have received considerable attention in recent years owing to the wealth of information they may provide regarding the strength, direction, and location of magnetic sources within a sample at fine spatial scales. Such techniques are particularly powerful when used in tandem with conventional bulk moment magnetometry, as they yield complementary information that is key to understanding fine-scale magnetization carried by rocks. Of particular interest are techniques that operate on a scale ranging from several micrometers to several hundred micrometers, for which a sufficiently large number of grains is averaged (assuming single domain magnetite, a common rock-forming mineral) and meaningful paleomagnetic data can still be obtained while providing high-resolution characterization of the magnetic sources.

[3]   Magnetization imaging techniques in this category typically measure one component of the magnetic field at very close proximity on a plane above the geological sample. They must rely on solving a nonunique inverse problem to retrieve the magnetization distribution that gives rise to the measured field data. The nonuniqueness arises because there are an infinite number of solutions that produce the same observed magnetic field [*Baratchart et al.*, 2013]. However, incorporating as much information as possible regarding the specificities of the sample under analysis and particularities of the experimental setup can in many cases narrow the space of solutions and help select physically meaningful magnetization distributions. In fact, we show in *Baratchart et al.* [2013] that, under specific conditions (e.g., unidirectional magnetization), it is even

Additional supporting information may be found in the online version of this article. Matlab inversion code is available upon request.

[1]Department of Earth, Atmospheric, and Planetary Sciences, Massachusetts Institute of Technology, Cambridge, Massachusetts, USA.

[2]Centre de Recherche INRIA Sophia Antipolis - Méditerranée, Sophia-Antipolis, France.

[3]Center for Constructive Approximation, Department of Mathematics, Vanderbilt University, Nashville, Tennessee, USA.

Corresponding author: E. A. Lima, Department of Earth, Atmospheric, and Planetary Sciences, Massachusetts Institute of Technology, Cambridge, MA 02139, USA. (limaea@mit.edu)

possible to ensure uniqueness for the inverse problem in scanning magnetic microscopy (SMM) given that, in this application, there are no sources outside a well-defined region in space.

[4] For the aforementioned spatial scales, the predominant imaging technique is scanning magnetic microscopy, in which a geological sample—typically a thin section—is displaced horizontally underneath a fixed magnetic sensor by a high-precision scanning stage while the magnetic field is recorded [*Weiss et al.*, 2007a]. This is effectively equivalent to mapping the field on a plane above a fixed sample, with the advantage that the magnetic sensor experiences a constant background field that is easily subtracted from the measurements. SMM techniques have advanced significantly in the past few years owing to the availability of low-cost high-performance miniature magnetic sensors based on technologies such as giant magnetoresistance, giant magnetoimpedance, magnetic tunnel junction, and Hall effect, among others [e.g., *Hankard et al.*, 2009; *Kletetschka et al.*, 2013; *Uehara and Nakamura*, 2007; *Volk et al.*, 2008]. The field sensitivities of these sensors are orders of magnitude lower than those of superconducting quantum interference devices (SQUIDs), but this disadvantage can be partly offset by the ability to bring such sensors to less than a few tens of micrometers from the sample's surface (a factor of ~3–10 closer than the typical measuring height of SQUIDs) where the fields are stronger and better resolved.

[5] In this paper, we focus on an inversion technique tailored for SMM that can be readily applied to similar imaging techniques, such as magneto-optical imaging, with just a few minor modifications. In addition, scanning magnetic microscopy can be considered as an aeromagnetic survey performed at microscales over source distributions with no topography. However, there are some important key distinctions between SMM and aeromagnetic surveys: (i) the source distribution in SMM can often be accurately modeled as a planar two-dimensional layer; (ii) strictly speaking, SMM measures the field produced directly by the sample's remanent magnetization instead of variations in a background field (magnetic anomalies); (iii) sensor positioning is very accurate in SMM, and the vertical component of the magnetic field is typically measured in place of the total field or the vector field; (iv) no correction algorithm is required to bring all measurements to the same surface or to grid the data; and (v) both the horizontal and the vertical extents of the magnetization distribution of magnetic sources are finite and known in advance. In spite of these differences, much of the mathematical framework associated with the inverse problem is very similar, and readers may easily apply some of the results and discussion presented in this work to the inversion of aeromagnetic data.

[6] Our technique is best suited for samples that carry unidirectional or unidimensional (i.e., antipodal) magnetization distributions. Unidirectional magnetizations are naturally present in many rocks at the spatial scales involved in SMM, where most samples do not exceed 2.5 cm in diameter. For igneous rocks, it is unusual to encounter individual magmatic cooling units with such small spatial scales; most likely, the whole sample will be magnetized in a single direction. For sedimentary rocks, very slow deposition rates (<~10 cm/million years) are required for the recording of magnetic reversals across a couple of centimeters. In that

case, samples may occasionally contain unidimensional magnetization distributions [e.g., ferromanganese crusts *Oda et al.*, 2011]. For metamorphic rocks, they would most likely be either unidirectional or multidirectional, depending on what spatial range the processes the rock was subjected to take place. In addition to such natural occurrences, paleomagnetic studies routinely require that artificial unidirectional magnetizations be imparted to samples in a controlled way, so as to assess magnetic properties of the rock and its capability to record ancient magnetic fields.

[7] As is customary in the field of inverse problems, no single inversion technique is universally applicable or exhibits superior performance in all applications. In the case of scanning magnetic microscopy, different assumptions regarding properties of the magnetization distribution as well as the mathematical method chosen to perform the inversion make each technique suitable to tackle a specific subset of problems. Ultimately, the application at hand will determine which inversion technique is best suited to undertake the inversion. Here, we present an inversion technique in the Fourier domain to retrieve thin planar unidirectional magnetization distributions from magnetic field maps that incorporates specificities of SMM.

[8] Techniques in the Fourier domain for inverting magnetic data have been extensively utilized since the late 1960s—particularly following the development of the fast Fourier transform (FFT) algorithm [*Cooley and Tukey*, 1965]—owing to significant gains provided in algorithm speed and less stringent memory requirements compared to spatial-domain techniques. However, this comes at a price: incorporating additional constraints—for example, nonnegativity and sample shape ("support")—is very hard or even infeasible in some cases. Furthermore, Fourier techniques require that the magnetic field be measured over larger areas. Pioneering applications included inversion of satellite data (using Fourier series) [*Mayhew*, 1979], magnetic anomaly data from irregular layers [*Parker*, 1973; *Parker and Huestis*, 1974], and marine magnetic anomalies from planar layers [*Bott*, 1967; *Schouten and McCamy*, 1972]. Whereas such techniques for inverting geomagnetic data have continued to be developed and improved in the past decades, the vast majority are not directly applicable to scanning magnetic microscopy owing to assumptions regarding properties of the source distribution (e.g., infinite layers with irregular topography are not suitable models for thin sections). An exception is the technique described in *Mareschal* [1985] for the inversion of potential field data that was later adapted specifically for scanning magnetic microscopy [*Egli and Heller*, 2000]. Although the latter work has yielded the first inversions of scanning SQUID microscopy maps of geological samples, experimental measurements were highly contaminated with position noise owing to precision issues in the scanning stage used. This ultimately impacted the data processing and the choice of regularization method, leading to a larger degree of regularization required to stabilize the inverse computations.

[9] A parallel path for the development of inversion techniques in the Fourier domain has been the reconstruction of planar electrical current distributions in conducting media from magnetic field measurements, with applications in biomagnetism and nondestructive testing [*Dallas*, 1985; *Kullmann and Dallas*, 1987; *Roth et al.*, 1989]. Although
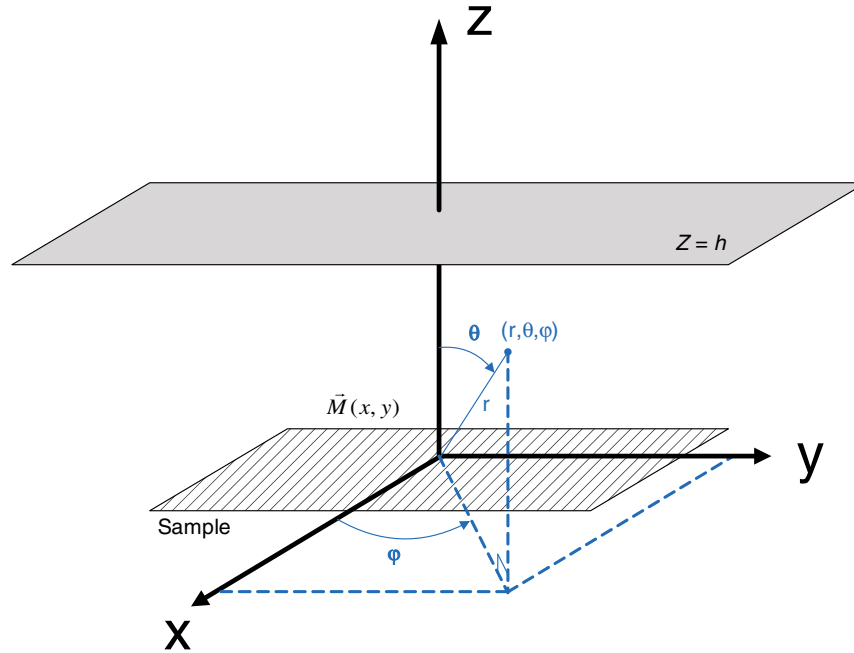
Figure 1. Measurement configuration assumed for the modeling. The magnetic field produced by a planar sample (hatched surface) with magnetization $\vec{M}$ and located on the horizontal plane $z = 0$ is measured on the plane $z = h$ parallel to the sample. The convention adopted for spherical coordinates is also indicated.

in this case the goal is to invert the Biot-Savart law, much of the mathematical formalism is somewhat similar to the case of imaging remanent magnetization. In fact, one of those techniques was adapted for reconstructing two-dimensional magnetization and susceptibility distributions [*Tan et al.*, 1996]. Hybrid techniques have also been developed to take advantage of useful features in both spatial and Fourier domains. One example is the Subtractive Optimally Localized Averages, which was initially developed for inversion of helioseismic data and has been recently adapted to scanning magnetic microscopy [*Usui et al.*, 2012]. In this technique, certain calculations are performed in the Fourier domain to improve speed while avoiding handling idiosyncrasies of Fourier transforms.

[10] We built our technique upon the pioneering works of *Egli and Heller* [2000], *Roth et al.* [1989], and *Tan et al.* [1996]. We achieved speeds up to several orders of magnitude faster than spatial-domain inversion algorithms [e.g., *Weiss et al.*, 2007a further optimized for superior performance], obtaining solutions for magnetization models with more than 15,000 source elements in just a few seconds. Like similar techniques in the Fourier domain, our inversion algorithm allows for a finer model discretization, thereby frequently yielding reliable higher-resolution estimates of magnetization distributions. To attain superior performance, we utilized additional two-dimensional signal processing methods to regularize the inverse problem, tame noise amplification, and improve nonnegativity. Because of its speed and accuracy, our technique is particularly powerful when multiple inversions of the same field map must be calculated so as to find the magnetization direction (if unknown) or to optimize regularization.

[11] Many of the Fourier techniques for the inversion of magnetic data previously described in the literature often lacked systematic strategies to identify and minimize the various sources of inversion degradation, which is especially critical when inverting nonideal data associated with geological samples measured with real magnetic sensors. In this work, we present a quantitative study showing the spatial distribution of error in the recovery and making use of an error metric to evaluate the overall mismatch when inverting synthetic data. In particular, we used synthetic test sources containing jump discontinuities, for which reconstructions are especially challenging in the Fourier domain owing to the Gibbs phenomenon. This allowed us not only to thoroughly characterize the inaccuracies in the solution under worst case conditions but also to assess the effectiveness of strategies to decrease recovery error. In addition, unlike some previous techniques, our method is optimized to yield solutions that are not excessively smoothed (excessive regularization) and to lack artifacts and high-frequency components of no physical significance. Furthermore, we characterize the class of magnetically silent sources (annihilators) that affects uniqueness in this particular type of inverse problem.

[12] Obtaining reliable solutions to ill-posed inverse problems typically requires a detailed understanding of all the factors that might affect the accuracy of the solution. Unfortunately, there does not seem to exist a simple recipe that would always lead to good results, except in very few particular cases. Here, we attempt to (i) present in an accessible form the basic theory of inversions in the Fourier domain of magnetic data from unidirectional magnetizations, as well as the main factors that impact inversion quality (section 2 and Appendices A and B), and (ii) progressively validate the results, starting with simulated and synthetic samples, where much information is known beforehand and can be independently verified, and closing with examples of actual geological samples (section 3).

2. Theory

2.1. The Inverse Problem for Scanning Magnetic Microscopy

[13] The external magnetic field $\overrightarrow{B}$ at position $\overrightarrow{r}$ generated by an arbitrary two-dimensional magnetization distribution $\overrightarrow{M}$ (moment per unit area) of finite size is given by

$$\overrightarrow{B}\left(\overrightarrow{r}\right) = (\mu_0/4\pi) \iint_S \left\{ \frac{3\overrightarrow{M}\left(\overrightarrow{r}'\right) \cdot \left(\overrightarrow{r} - \overrightarrow{r}'\right)}{|\overrightarrow{r} - \overrightarrow{r}'|^5}\left(\overrightarrow{r} - \overrightarrow{r}'\right) - \frac{\overrightarrow{M}\left(\overrightarrow{r}'\right)}{|\overrightarrow{r} - \overrightarrow{r}'|^3} \right\} d\overrightarrow{r}'', \tag{1}$$

where S is the magnetization surface, μ_0 is the permeability of free space, and $\overrightarrow{r}'$ denotes the coordinates of a magnetization element.

[14] This is a realistic model for SMM, in which doubly polished $30\,\mu m$ thin sections of geological samples are typically measured at distances greater than three times the sample thickness [*Fong et al.*, 2005; *Weiss et al.*, 2007a]. We assume that the magnetic field is measured on the plane $z = h$ parallel to a sample located on the *x-y* horizontal plane, where *h* is the sensor-to-sample distance or liftoff (Figure 1). By incorporating the integration limits into $\overrightarrow{M} = (M_x, M_y, M_z)$, we can express equation (1) as two-dimensional convolutions of magnetization components with Green's functions that describe the source-measurement configuration. After expanding equation (1) in Cartesian coordinates and extending the integration limits to infinity, the three components of $\overrightarrow{B}$ are:

$$B_x = (G_{xx} - G) * M_x + G_{xy} * M_y + G_{xz} * M_z, \tag{2}$$

$$B_y = G_{yx} * M_x + \left(G_{yy} - G\right) * M_y + G_{yz} * M_z, \tag{3}$$

$$B_z = G_{zx} * M_x + G_{zy} * M_y + (G_{zz} - G) * M_z, \tag{4}$$

where * denotes a two-dimensional convolution operation between two functions *U* and *V*

$$U(x,y) * V(x,y) = \int_{-\infty}^{+\infty} \int_{-\infty}^{+\infty} U(\eta, \xi) V(x - \eta, y - \xi) d\eta d\xi,$$

and where the Green's functions are given by

$$G_{xx} = \frac{\mu_0}{4\pi} \frac{3x^2}{\left(x^2 + y^2 + h^2\right)^{5/2}}; \quad G_{xy} = G_{yx} = \frac{\mu_0}{4\pi} \frac{3xy}{\left(x^2 + y^2 + h^2\right)^{5/2}};$$

$$G_{yy} = \frac{\mu_0}{4\pi} \frac{3y^2}{\left(x^2 + y^2 + h^2\right)^{5/2}}; \quad G_{xz} = G_{zx} = \frac{\mu_0}{4\pi} \frac{3xh}{\left(x^2 + y^2 + h^2\right)^{5/2}};$$

$$G_{zz} = \frac{\mu_0}{4\pi} \frac{3h^2}{\left(x^2 + y^2 + h^2\right)^{5/2}}; \quad G_{yz} = G_{zy} = \frac{\mu_0}{4\pi} \frac{3yh}{\left(x^2 + y^2 + h^2\right)^{5/2}};$$

$$G = \frac{\mu_0}{4\pi} \frac{1}{\left(x^2 + y^2 + h^2\right)^{3/2}}.$$

$$\tag{5}$$

[15] Notice that the nine double-indexed Green's functions are associated with the first term within curly braces in equation (1), while the Green's function *G* stems from the second term.

(As was done in equations (2)–(5), we will often denote the field measured on the plane $z = h$ by $\overrightarrow{B}(x, y)$ or just $\overrightarrow{B}$ instead of $\overrightarrow{B}(x, y, h)$, so as to simplify the notation. Similarly, the Green's functions and magnetization distributions will often be denoted by their abbreviated form. This double-indexed notation indicates the influence of a specific magnetization component on a particular magnetic field component and should not be confused with the notation commonly used in mathematics to denote partial derivatives.)

[16] To estimate the magnetization distribution from magnetic field measurements, we need to invert (i.e., deconvolve) equations (2)–(4) for $\overrightarrow{M}$. It is often beneficial to perform this operation in the Fourier domain, where convolutions are transformed into products. Taking the two-dimensional Fourier transform of equations (2)–(4) yields

$$b_x = (g_{xx} - g)m_x + g_{xy}m_y + g_{xz}m_z; \tag{6}$$

$$b_y = g_{xy}m_x + \left(g_{yy} - g\right)m_y + g_{yz}m_z; \tag{7}$$

$$b_z = g_{xz}m_x + g_{yz}m_y + (g_{zz} - g)m_z, \tag{8}$$

where

$$g_{xx} - g = \begin{cases} -(\mu_0/2)\dfrac{\kappa_x^2}{\kappa}e^{-h\kappa} & , \text{if } \kappa \neq 0; \\ 0 & , \text{if } \kappa = 0 \end{cases} \tag{9}$$

$$g_{xy} = \begin{cases} -(\mu_0/2)\dfrac{\kappa_x\kappa_y}{\kappa}e^{-h\kappa} & , \text{if } \kappa \neq 0; \\ 0 & , \text{if } \kappa = 0 \end{cases} \tag{10}$$

$$g_{yy} - g = \begin{cases} -(\mu_0/2)\dfrac{\kappa_y^2}{\kappa}e^{-h\kappa} & , \text{if } \kappa \neq 0; \\ 0 & , \text{if } \kappa = 0 \end{cases} \tag{11}$$

$$g_{xz} = -(\mu_0/2)i\kappa_x e^{-h\kappa}; \tag{12}$$

$$g_{zz} - g = (\mu_0/2)\kappa e^{-h\kappa}; \tag{13}$$

$$g_{yz} = -(\mu_0/2)i\kappa_y e^{-h\kappa}, \tag{14}$$

i is the imaginary unit, $\kappa = \sqrt{\kappa_x^2 + \kappa_y^2}$ is the radial spatial frequency (wave number), and κ_x and κ_y are the spatial frequencies in the *x* and *y* directions, respectively.

[17] Here, we have used the following definition of the Fourier transform pair $H(x,y)$, $h(\kappa_x, \kappa_y)$:

$$h\left(\kappa_x, \kappa_y\right) = \int_{-\infty}^{+\infty} \int_{-\infty}^{+\infty} H(x,y)e^{-i\left(\kappa_x x + \kappa_y y\right)}dx\,dy; \tag{15}$$

$$H(x,y) = \frac{1}{(2\pi)^2} \int_{-\infty}^{+\infty} \int_{-\infty}^{+\infty} h\left(\kappa_x, \kappa_y\right)e^{i\left(\kappa_x x + \kappa_y y\right)}d\kappa_x\,d\kappa_y. \tag{16}$$

[18] We may also denote the Fourier transform of a function *H* by $\mathcal{F}\{H\}$ and the inverse transform by $\mathcal{F}^{-1}\{h\}$.

[19] Notice that equations (6)–(8) express algebraic relationships between functions of κ_x and κ_y rather than between numbers. Furthermore, for each point (κ_x,κ_y) in the spatial frequency plane, there is an associated 3×3 system of linear equations

$$
\begin{bmatrix}
(g_{xx} - g)(\kappa_x, \kappa_y) & g_{xy}(\kappa_x, \kappa_y) & g_{xz}(\kappa_x, \kappa_y) \\
g_{xy}(\kappa_x, \kappa_y) & (g_{yy} - g)(\kappa_x, \kappa_y) & g_{yz}(\kappa_x, \kappa_y) \\
g_{xz}(\kappa_x, \kappa_y) & g_{yz}(\kappa_x, \kappa_y) & (g_{zz} - g)(\kappa_x, \kappa_y)
\end{bmatrix}
\begin{bmatrix}
m_x(\kappa_x, \kappa_y) \\
m_y(\kappa_x, \kappa_y) \\
m_z(\kappa_x, \kappa_y)
\end{bmatrix}
=
\begin{bmatrix}
b_x(\kappa_x, \kappa_y) \\
b_y(\kappa_x, \kappa_y) \\
b_z(\kappa_x, \kappa_y)
\end{bmatrix},
\tag{17}
$$

or $\underline{\underline{\mathcal{G}}}\underline{m} = \underline{b}$. Substituting equations (9)–(14), we get

$$
\underline{\underline{\mathcal{G}}}(\kappa_x, \kappa_y) = -\frac{\mu_0}{2}e^{-h\kappa}(i\kappa_x, i\kappa_y, -\kappa)^T(-i\kappa_x/\kappa, -i\kappa_y/\kappa, 1)
$$

$$
= \begin{cases}
-\frac{\mu_0}{2}e^{-h\kappa}
\begin{bmatrix}
\kappa_x^2/\kappa & \kappa_x\kappa_y/\kappa & i\kappa_x \\
\kappa_x\kappa_y/\kappa & \kappa_y^2/\kappa & i\kappa_y \\
i\kappa_x & i\kappa_y & -\kappa
\end{bmatrix}
, & \text{if } \kappa \neq 0. \\[2em]
\underline{\underline{0}} & \text{if } \kappa = 0.
\end{cases}
\tag{18}
$$

[20] It is easy to verify that the symmetric matrix $\underline{\underline{\mathcal{G}}}$ is singular (i.e., not invertible) with rank 1 for every $(\kappa_x,\kappa_y) \neq (0,0)$. This suggests that, in general, arbitrary two-dimensional magnetization distributions cannot be uniquely recovered from magnetic field maps, even if all three components of the field are known everywhere on a plane. (In some cases, sophisticated spectral/spatial unmixing techniques can be employed to tackle nonuniqueness when attempting to invert multidirectional magnetization distributions [*Baratchart et al.*, 2013], but such an approach is outside of the scope of this paper.) In addition, it shows that, for low or moderate noise levels, a single field component carries all the information about the magnetization distribution [*Lima and Weiss*, 2009]. For $\kappa = 0$, $\underline{\underline{g}}$ is the zero matrix, which implies that the uniform (constant) component of the magnetization distribution cannot be directly recovered from magnetic field measurements. This is not surprising, since uniform planar magnetizations with support in the entire plane constitute a classic example of magnetically silent source or annihilator [*Baratchart et al.*, 2013; *Parker*, 1977], generating no external magnetic field. Thus, a constant magnetization can always be added to the solution without changing the field produced by the overall distribution. We will show later that this will not be a serious issue, provided we restrict our sources to finite-size distributions (which, of course, is always what is encountered in practical applications of SMM) and we map the magnetic field over a plane with horizontal dimensions larger than the sample's horizontal dimensions.

[21] The fact that $\underline{\underline{g}}$ is rank 1 prompts the question of whether a magnetization distribution with a single free parameter can be uniquely recovered—except for its uniform part—from measurements of a single magnetic field component. The most interesting practical case consists of a unidirectional magnetization distribution with known fixed direction but variable strength [*Baratchart et al.*, 2013; *Weiss et al.*, 2007a]. Retrieving such a magnetization from scanning magnetic microscopy data measured on a plane above the sample is the goal of this paper.

[22] Before proceeding, we remark that although the physical magnetization distributions considered here have finite dimensions (i.e., compact support), any inversion model implemented in the Fourier domain implicitly assumes that magnetizations may have infinite (unbounded) support. This is of special significance because we show in a companion article that there is no silent source with compact support that is also unidirectional [*Baratchart et al.*, 2013]. We will show later how compact support constraints can be indirectly incorporated into the inversion.

2.2. Unidirectional Model

[23] If we assume the direction of the magnetization distribution is everywhere the same, $\vec{M}$ may be expressed as

$$
\vec{M}(x,y) = M(x,y)\hat{n},
\tag{19}
$$

where $\hat{n} = \sin(\theta)\cos(\varphi)\hat{x} + \sin(\theta)\sin(\varphi)\hat{y} + \cos(\theta)\hat{z}$ is a fixed unit vector representing the direction of the magnetization, and θ and φ are the conventional zenith and azimuth angles in spherical coordinates (i.e., $\theta = 0$ represents the $+z$ direction, whereas $\theta = \pi/2$, $\varphi = 0$ represents the $+x$ direction—see Figure 1). If M is nonnegative for all (x, y), then $\vec{M}$ is called *unidirectional*. More generally, without any restrictions of sign, we say that a magnetization $\vec{M}$ of the form (19) is *unidimensional*. While the focus of this paper is on unidirectional magnetizations because they naturally arise in geoscience applications, the techniques described herein apply as well in the unidimensional case.

[24] Substituting equation (19) in equations (2)–(4), we get

$$
B_x = (G_{xx} - G) * (M\sin\theta\cos\varphi) + G_{xy} * (M\sin\theta\sin\varphi) + G_{xz} * (M\cos\theta),
\tag{20}
$$

$$
B_y = G_{yx} * (M\sin\theta\cos\varphi) + (G_{yy} - G) * (M\sin\theta\sin\varphi) + G_{yz} * (M\cos\theta),
\tag{21}
$$

$$
B_z = G_{zx} * (M\sin\theta\cos\varphi) + G_{zy} * (M\sin\theta\sin\varphi) + (G_{zz} - G) * (M\cos\theta).
\tag{22}
$$

Table 1. Conditions for Breakdown of Inversions of Unidirectional Planar Magnetizations

Component	Condition #1	Condition #2	Condition #3
b_x	$\kappa_x = \kappa_y = 0$	$\kappa_x = 0$	$\theta = \pi/2; (\cos\varphi)\kappa_x + (\sin\varphi)\kappa_y = 0$
b_y	$\kappa_x = \kappa_y = 0$	$\kappa_y = 0$	$\theta = \pi/2; (\cos\varphi)\kappa_x + (\sin\varphi)\kappa_y = 0$
b_z	$\kappa_x = \kappa_y = 0$	N/A	$\theta = \pi/2; (\cos\varphi)\kappa_x + (\sin\varphi)\kappa_y = 0$

[25] In the Fourier domain, the above equations become, after substituting equations (9)–(14):

$$b_x(\kappa_x, \kappa_y) = -\frac{\mu_0}{2} e^{-h\kappa} \left[\left(\frac{\kappa_x^2}{\kappa} \right) \sin\theta \cos\varphi + \left(\frac{\kappa_x \kappa_y}{\kappa} \right) \sin\theta \sin\varphi \right.$$
$$\left. + (i\kappa_x) \cos\theta \right] m(\kappa_x, \kappa_y), \tag{23}$$

$$b_y(\kappa_x, \kappa_y) = -\frac{\mu_0}{2} e^{-h\kappa} \left[\left(\frac{\kappa_x \kappa_y}{\kappa} \right) \sin\theta \cos\varphi + \left(\frac{\kappa_y^2}{\kappa} \right) \sin\theta \sin\varphi \right.$$
$$\left. + (i\kappa_y) \cos\theta \right] m(\kappa_x, \kappa_y), \tag{24}$$

$$b_z(\kappa_x, \kappa_y) = -\frac{\mu_0}{2} e^{-h\kappa} \left[(i\kappa_x) \sin\theta \cos\varphi + (i\kappa_y) \sin\theta \sin\varphi \right.$$
$$\left. - (\kappa) \cos\theta \right] m(\kappa_x, \kappa_y). \tag{25}$$

[26] Notice that equations (23) and (24) are only defined for $\kappa \neq 0$, whereas the following trivial relationships hold for $\kappa = 0$:

$$b_x(0,0) = 0; \quad b_y(0,0) = 0; \quad b_z(0,0) = 0, \tag{26}$$

which express the fact that the mean values of each field component (and, consequently, of the vector field) are zero.

[27] Inversion of equations (23)–(25) for m is only possible at spatial frequencies where the terms within square brackets are not equal to zero. Let us begin by analyzing b_x. In this case, the conditions for inversion breakdown (in addition to $\kappa = 0$) are:

$$\kappa_x \left[\kappa_x \sin\theta \cos\varphi + \kappa_y \sin\theta \sin\varphi + (i\kappa) \cos\theta \right] = 0. \tag{27}$$

[28] We notice that equation (23) breaks down whenever just $\kappa_x = 0$, independently of the values θ and φ might assume (i.e., for any arbitrary magnetization direction). To determine the remaining breakdown conditions—which are associated with the term within square brackets in equation (27)—it is convenient to define rotated spatial frequency variables κ_u and κ_v as follows

$$\begin{cases} \kappa_u = (\cos\varphi)\kappa_x + (\sin\varphi)\kappa_y \\ \kappa_v = (-\sin\varphi)\kappa_x + (\cos\varphi)\kappa_y \\ \kappa' = \sqrt{\kappa_u^2 + \kappa_v^2} = \kappa, \end{cases} \tag{28}$$

which are rotated by the azimuth angle φ with respect to the pair κ_x, κ_y. This embeds in the rotated variables the dependence on

φ, simplifying the equations. Substituting equation (28) into equation (27), and performing some manipulations, we get

$$i\kappa_u \sin\theta = \kappa' \cos\theta. \tag{29}$$

[29] Now, the only way an imaginary number can equal a real number is if both numbers are zero. Thus, we have to solve two simultaneous equations

$$\begin{cases} \kappa_u \sin\theta = 0 \\ \kappa' \cos\theta = 0. \end{cases} \tag{30}$$

[30] The solutions are

$$\kappa' = 0 \quad \text{(for arbitrary } \theta\text{)}, \tag{31}$$

and

$$\kappa_u = 0 \quad \text{and} \quad \theta = \pi/2. \tag{32}$$

[31] The breakdown condition expressed by equation (31) was already obtained above (i.e., $\kappa = 0$). Equation (32), on the other hand, shows that for any magnetization direction that is purely horizontal, equation (23) breaks down along the line $(\cos\varphi)\kappa_x + (\sin\varphi)\kappa_y = 0$ (which is perpendicular to the magnetization direction) in the frequency plane. The conditions for b_y are similar, but equation (24) breaks down for $\kappa_y = 0$, instead of $\kappa_x = 0$. As for b_z, equation (25) breaks down only at $\kappa = 0$ and, for $\theta = \pi/2$, at $(\cos\varphi)\kappa_x + (\sin\varphi)\kappa_y = 0$. Table 1 summarizes the conditions associated with each field component.

[32] The fact that inversion of the z field component breaks down in a narrower range is very significant, as it opens the possibility for obtaining high-quality magnetization estimates from z component magnetic field maps, particularly for distributions that are not magnetized in the sample plane (horizontal). Therefore, we will henceforth focus on estimating magnetization distributions from maps of the z component of the magnetic field.

[33] It should be noticed that all the conditions shown in Table 1 are intrinsic to the magnetic inverse problem and cannot be avoided no matter which component (or combination of the three components) of the field is used. These conditions do not mean that an inverse solution cannot be obtained, but rather that there are information losses associated with them. This means that something will be missing in the solution when these conditions are met. For $\kappa = 0$, it means all solutions to this inverse problem may possibly be off by a constant factor which is associated with the uniform planar magnetization silent source. As detailed in Appendix B, this will not be a serious impediment for scanning magnetic microscopy data, since the constant factor may be obtained by carrying out a few additional calculations so as to ensure the solution has compact support. Regarding the condition $\theta = \pi/2$; $(\cos\varphi)\kappa_x + (\sin\varphi)\kappa_y = 0$, it implies that purely in-plane magnetizations cannot be faithfully recovered—without imposing further constraints—even after correcting for the constant factor. Specifically, the estimated magnetization will lack accurate information at spatial frequencies along the line $(\cos\varphi)\kappa_x + (\sin\varphi)\kappa_y = 0$. This is usually manifested in the solution as undulations perpendicular to the magnetization direction $\hat{n}$. Such information losses may be partially mitigated by regularization techniques, although sometimes this improvement comes at the expense of reduced spatial resolution.
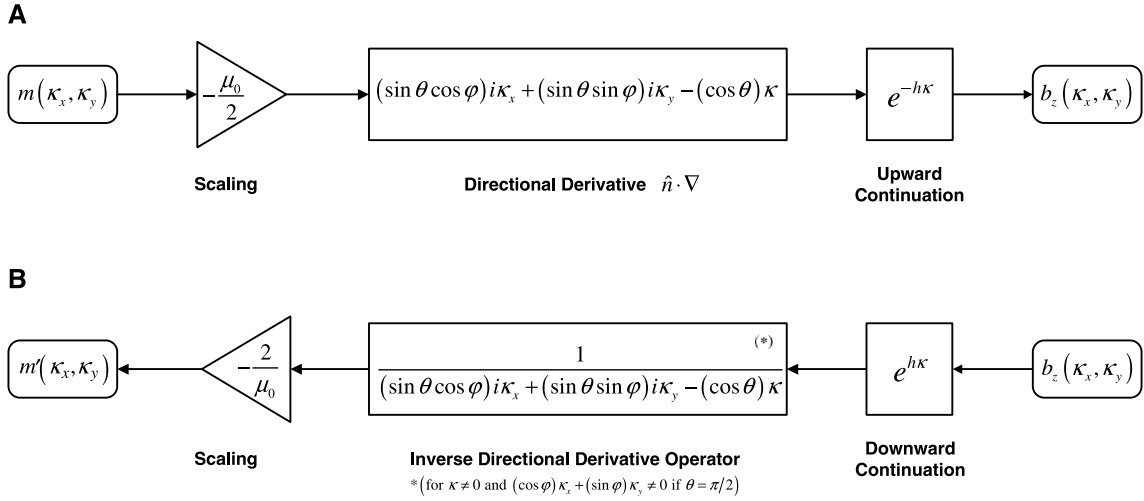
A

B

Figure 2. The operator mapping planar magnetization distributions into magnetic field maps viewed as the composition of three operations. (a) Forward operator comprised of scaling, directional derivative, and upward continuation operations. (b) Inverse operator comprised of scaling, inverse directional derivative, and downward continuation operations. Because the operator is linear and translation invariant, the order in which the operations are performed is unimportant.

[34] Another way of interpreting this condition is realizing that in-plane unidirectional magnetizations whose intensities do not vary along the magnetization direction $\hat{n}$ are also silent sources. In fact, one can use equation (1) to demonstrate that any in-plane magnetization of the form $\vec{M}(x,y) = M(v)\hat{d}$— where $\hat{d} = (\cos\varphi)\hat{x} + (\sin\varphi)\hat{y}$, u and v are coordinates in a rotated coordinate system defined by $u = x\cos\varphi + y\sin\varphi$, $v = -x\sin\varphi + y\cos\varphi$, and M does not depend on u—gives rise to an integrand with odd symmetry, and, consequently, no external magnetic field is produced.

[35] Notice that each condition for breakdown of equations (23)–(25) in fact corresponds to a silent source for the vector field $\vec{B}$ or for one of its horizontal components. In particular, whereas each silent source for the z component of $\vec{B}$ (i.e., conditions 1 and 3 in Table 1) is also a silent source for the x and y components, the converse is not true for this specific inverse problem (i.e., conditions 2 for B_x and B_y do not make $B_z = 0$). That is to say, a null z component of the field over the whole measurement plane implies $\vec{B} = \vec{0}$, but a null x- or y- component map does not. For this reason, the field component perpendicular to the sample plane is the most advantageous of the three components for inversion in this source-sensor configuration. A very important result is that the conditions listed in Table 1 for the unidirectional case all correspond to silent sources with infinite support, as they are constant along one direction at least. In fact, the inverse problem for unidirectional magnetization distributions with compact support is *unique* irrespective of the magnetization direction [*Baratchart et al.*, 2013].

[36] To illustrate these points, we show in Fig. S1 (in supporting information) two examples of magnetization distributions that produce a nonzero magnetic field with a single silent horizontal field component. In the first case, the synthetic distribution consisted of three infinitely long strips parallel to the x axis, each uniformly magnetized in a different direction. The z and y components are nonzero,

whereas the x component is silent. Because conditions 2 for B_x and B_y do not depend on the magnetization direction, each strip yields $B_x = 0$ everywhere. In the second case, the synthetic distribution consisted of three infinitely long strips parallel to the y axis, each uniformly magnetized in a different direction and yielding $B_y = 0$ everywhere. Here, the z and x components are nonzero, whereas the y component is silent.

2.3. Inversion

[37] In view of the existence of silent sources with infinite (unbounded) support, the inversion of equation (25) calls for a careful approach. For example, the estimate of the magnetization m' obtained via

$$m'(\kappa_x, \kappa_y) = -\frac{2}{\mu_0}e^{h\kappa}\left[(i\kappa_x)\sin\theta\cos\varphi + (i\kappa_y)\sin\theta\sin\varphi\right.$$

$$\left. - (\kappa)\cos\theta\right]^{-1}b_z(\kappa_x,\kappa_y) \qquad (33)$$

will most likely not resemble the real magnetization at all because the reciprocal of the term within square brackets is not defined at certain spatial frequencies.

[38] Let us dissect equation (25) to better understand how the inversion fails and what could be done to properly invert the magnetic field data. We observe that equation (25) may be regarded as the composition of three different operations (Figure 2A): (i) scaling, (ii) directional derivative [*Blakely*, 1996], and (iii) upward continuation. [The directional derivative term stems from the fact that multiplying the Fourier transform of a harmonic function by $i\kappa_x$, $i\kappa_y$, or $-\kappa$ corresponds to taking the partial derivatives $\partial/\partial x$, $\partial/\partial y$, or $\partial/\partial z$, respectively, in the spatial domain. Thus, taking the directional derivative $\nabla H \cdot \hat{n}$ of a harmonic function H along an arbitrary direction $\hat{n} = \sin(\theta)\cos(\varphi)\hat{x} + \sin(\theta)\sin(\varphi)\hat{y} + \cos(\theta)\hat{z}$ is equivalent to multiplying its Fourier transform by $(i\kappa_x)\sin\theta\cos\varphi + (i\kappa_y)\sin\theta\sin\varphi - (\kappa)\cos\theta$.] Likewise, equation (33) may be considered as the
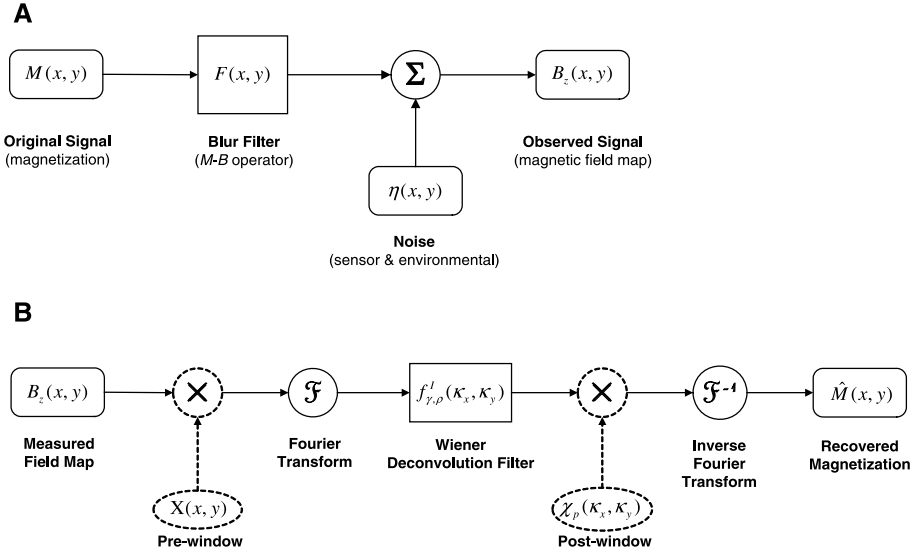
A

B

Figure 3. (a) Problem formulation for Wiener deconvolution. The original signal (two-dimensional magnetization distribution) is degraded by the blur filter [operator mapping magnetizations $M(x,y)$ into magnetic field maps $B_z(x,y)$] and by additive noise $\eta(x,y)$ (sensor and environmental noise components), resulting in the observed signal (map of the vertical field component B_z). Wiener deconvolution essentially estimates M from B_z by calculating an inverse filter that prevents excessive noise amplification. (b) Schematic depicting various steps of the inversion procedure. Dashed lines represent optional operations to reduce mapping area artifacts and improve nonnegativity. A measured field map $B_z(x,y)$ is multiplied by a window function $X(x,y)$ (prewindowing) prior to the computation of the two-dimensional Fourier transform. This transformed signal is first multiplied by the Wiener deconvolution filter (or by the split regularization deconvolution filter) and subsequently multiplied by a window function $\chi_p(\kappa_x,\kappa_y)$ (postwindowing). Finally, the inverse Fourier transform is applied resulting in the estimated recovered magnetization $\hat{M}(x,y)$.

composition of the individual inverse operations (i.e., inverse filters) (Figure 2B). This decomposition of the magnetic inverse problem arises naturally when an equivalent formulation based on the magnetic scalar potential ϕ is used, and the inversion is split into two parts [*Baratchart et al.*, 2013]: $B_z \to \phi$, and $\phi \to M$. Considering that the operator transforming planar magnetization distributions into magnetic field maps is both linear and translation invariant—as given by equation (1)—the order in which these steps are performed is not critical. Thus, each step may be viewed as the application of a corresponding spatial filter on a two-dimensional signal and can be analyzed separately.

[39] Two of those inverse operations are potentially troublesome for different reasons. First, while upward continuation is a bijective mapping (i.e., a one-to-one correspondence)—and therefore invertible on its range—its exponential dependence on κ poses a well-known problem in practical applications, namely the large amplification of the spectrum at high spatial frequencies carried out by the downward (inverse) operator, drastically exacerbating noise and mapping area artifacts as frequency increases [*Huestis and Parker*, 1979]. Second, as discussed in section 2.2, inversion of the directional derivative operator is not possible everywhere: the directional derivative operator is always zero at the origin (condition #1) and for $\theta = \pi/2$, along the line $(\cos \varphi)\kappa_x + (\sin \varphi)\kappa_y = 0$ (condition #3). In effect, as these singularities are approached, the inverse operator grows without bound, leading to large amplification of the frequency spectrum in regions around the singularities. Notice

that, unlike the downward continuation operator, excessive magnification also takes place at low spatial frequencies in this case.

2.4. Regularization

[40] Regularization must be introduced to stabilize the inversion by taming excessive noise amplification and by assigning a value to the inverse filter at spatial frequencies where equation (25) is zero. Several approaches may be used, each with advantages and shortcomings. Here, we analyze two regularization schemes that have yielded good results for SQUID microscopy data and that help illustrate some of the issues associated with this type of magnetic inverse problem: parametric Wiener deconvolution and split regularization.

[41] In our case, Wiener deconvolution simultaneously regularizes the downward continuation and inverse directional derivative operators, whereas split regularization regularizes them in separate steps. In particular, the basic idea behind Wiener regularization is to find a function $\psi_W(\kappa_x,\kappa_y)$ that approximates $-\frac{2}{\mu_0} e^{h\kappa} \left[(i\kappa_x) \sin\theta \cos\varphi + (i\kappa_y) \sin\theta \sin\varphi - (\kappa) \cos\theta \right]^{-1}$ such that $\hat{m}(\kappa_x,\kappa_y) = \psi_W(\kappa_x,\kappa_y) b_z(\kappa_x,\kappa_y)$ is devoid of excessive noise amplification and other inversion artifacts. ($\hat{m}$ denotes an estimate for the Fourier transform m of the true magnetization.) For split regularization, the goal is to find two functions $\psi_{S1}(\kappa_x,\kappa_y)$ and $\psi_{S2}(\kappa_x,\kappa_y)$ that can be adjusted independently while approximating $e^{h\kappa}$ and $-(2/\mu_0)[(i\kappa_x) \sin\theta \cos\varphi + (i\kappa_y)\sin\theta \sin\varphi - (\kappa)\cos\theta]^{-1}$, respectively, so

as to tame artifacts in $\hat{m}\left(\kappa_x, \kappa_y\right) = \psi_{S1}\left(\kappa_x, \kappa_y\right)\psi_{S2}\left(\kappa_x, \kappa_y\right)b_z$ $\left(\kappa_x, \kappa_y\right)$. The functions ψ_W, ψ_{S1}, and ψ_{S2} are adjusted by means of parameters to control the trade-off between accuracy in the inversions and artifact subduing.

2.4.1. Parametric Wiener Deconvolution

[42] Wiener deconvolution is often utilized to regularize the associated ill-posed inverse problem when implementing deconvolutions in the presence of additive noise [*Jain*, 1989; *Lim*, 1990]. To use Wiener deconvolution in our problem, we regard the mapping of magnetizations into field maps as a two-dimensional linear filter that distorts the original signal (i.e., the magnetization distribution). Additive noise may further degrade it, resulting in a "blurred" observed signal (i.e., the associated field map) that is recorded by the scanning magnetic microscope (Figure 3A). In essence, Wiener deconvolution implements an approximation to the inverse operator by way of a spatial filter that attenuates growth at frequencies with poor signal-to-noise ratios (SNRs). It minimizes the mean square error (MSE) between the original (true) magnetization M and the recovered one $\hat{M}$, which is defined as $E\left\{\left[M(x,y) - \hat{M}(x,y)\right]^2\right\}$, where E denotes the expected value of a random variable. Clearly, the true magnetization is not known in advance, and some of its statistical properties should instead be estimated or postulated. Minimization of the MSE ensures that the recovered magnetization is as close as possible to the original one in a statistical sense. Therefore, there is no guarantee that a particular solution obtained will be nonnegative (i.e., strictly unidirectional). However, as we will see later, further processing may very often improve nonnegativity.

[43] If $f(\kappa_x, \kappa_y)$ represents the two-dimensional blur filter [i.e., the operator that maps a unidirectional magnetization on the x-y plane into the z component of the magnetic field on the horizontal plane $z = h$, as in equation (25)], the Wiener deconvolution filter becomes

$$f^I\left(\kappa_x, \kappa_y\right) = \frac{\overline{f}\left(\kappa_x, \kappa_y\right)s_{mm}\left(\kappa_x, \kappa_y\right)}{\left|f\left(\kappa_x, \kappa_y\right)\right|^2 s_{mm}\left(\kappa_x, \kappa_y\right) + s_{\eta\eta}\left(\kappa_x, \kappa_y\right)}, \quad (34)$$

where an overbar denotes a complex conjugation operation, s_{mm} stands for the power spectral density (PSD) of the magnetization, $s_{\eta\eta}$ stands for the PSD of the additive noise $\eta(x,y)$, and f is given by

$$f\left(\kappa_x, \kappa_y\right) = -\frac{\mu_0}{2}e^{-h\kappa}\left[\left(i\kappa_x\right)\sin\theta\cos\varphi + \left(i\kappa_y\right)\sin\theta\sin\varphi - (\kappa)\cos\theta\right].$$
$$(35)$$

[44] (The PSD is the Fourier transform of the autocorrelation function R_{HH}, which is defined as $E\left\{H(x,y)\overline{H}(x + \xi, y + \psi)\right\}$, where H stands for an arbitrary stationary stochastic process. For ergodic stochastic processes, the autocorrelation can be estimated by means of the formula $R_{HH}(\eta, \xi) =$

$$\lim_{X\to\infty}\lim_{Y\to\infty}(4XY)^{-1}\int_{-X}^{X}\int_{-Y}^{Y}H(x,y)\overline{H}(x + \eta, y + \xi)dxdy.)$$

[45] The Wiener deconvolution filter in equation (34) essentially implements a compromise between high-pass filtering (i.e., inverse filtering for deblurring) and low-pass filtering (i.e., noise smoothing) that is determined by the SNR at each spatial frequency. At frequencies contaminated with high levels of noise, inverse filtering is reduced, and low-pass filtering prevails to decrease noise. In regions where noise level is low compared to the signal, the Wiener deconvolution filter approaches the inverse filter.

[46] Three underlying assumptions associated with Wiener filtering require particular attention in our case: (i) all two-dimensional signals involved (i.e., magnetization distribution, additive noise component, and field map) must have zero mean, (ii) the power spectra of the magnetization and the noise must both be known, and (iii) noise must be uncorrelated with the original magnetization (and, thus, with the field). Assumption (i) does not present a problem, as equation (26) guarantees that the mean value of the vector magnetic field of any finite-sized magnetization distribution with finite strength is zero. Of course, magnetic sensors that are unable to measure absolute magnetic field, as well as noise, drift, and asymmetrical mapping areas may create a small nonzero mean value, which can be easily fixed prior to performing a Wiener deconvolution.

[47] Regarding (ii), estimating the noise power spectrum is usually achievable, even when several noise components are present [i.e., flicker ($1/f$) noise, white noise, periodic noise]. One may compute a periodogram or utilize other suitable methods to estimate the PSD of the noise from a blank scan (i.e., a magnetic map obtained above a zero magnetization region). Alternatively, one may characterize the noise of the system in the time domain and then estimate the PSD of the spatial noise by incorporating the effects of both sampling and scanning operations.

[48] In contrast, estimating the power spectrum of the magnetization is not a simple task. Given that the magnetization distribution is precisely what we aim to reconstruct, there is not much detail we might know beforehand. (Note that, in fact, Wiener filtering requires knowledge of the PSD and not of the magnetization distribution itself.) Nevertheless, certain characteristics of the power spectrum may be postulated based on general assumptions regarding the source distribution.

[49] As for (iii), although most magnetic field sensors exhibit noise that is independent from the signal, some devices might display hysteresis under certain conditions. In addition, imprecision in the positioning of the x-y stage—the so-called position noise—often appears in the field map as a signal-dependent noise [*Lee et al.*, 2004]. Furthermore, windowing effects due to finite mapping areas and finite step sizes may also be regarded as signal-dependent noise [see Appendix A: the Fourier transform of the rectangle defining the mapping area is convolved with the (infinitely extended) magnetic field map]. Thus, while these effects may be minimized by careful sensor design and operation, enlarged mapping areas, and finer mapping grids, it is usually not possible to completely eliminate them.

[50] With respect to the inverse filter equation (34), coarsely estimating the PSDs s_{mm} and $s_{\eta\eta}$ leads to under- or overregularization of the solution, meaning that the calculated Wiener filter is no longer the optimal linear filter in the sense of minimum mean square error for the particular inverse problem at hand. Magnetization-correlated noise may also degrade the performance of the calculated optimum filter.

For these reasons, it is often expedient to utilize a parametric version of the Wiener filter to implement the deconvolution:

$$f_\gamma^I(\kappa_x, \kappa_y) = \frac{\overline{f}(\kappa_x, \kappa_y) s_{mm}(\kappa_x, \kappa_y)}{|f(\kappa_x, \kappa_y)|^2 s_{mm}(\kappa_x, \kappa_y) + \gamma s_{\eta\eta}(\kappa_x, \kappa_y)}, \quad (36)$$

where $\gamma > 0$ is a parameter that controls the amount of regularization introduced.

[51] The simplest implementation of the parametric Wiener deconvolution assumes that both the magnetization and the noise are white-noise stochastic processes [i.e., constant (unity) PSDs]. In this case, the Wiener filter simplifies to

$$f_\gamma^I(\kappa_x, \kappa_y) = \frac{\overline{f}(\kappa_x, \kappa_y)}{|f(\kappa_x, \kappa_y)|^2 + \gamma}. \quad (37)$$

[52] For $\gamma = 0$, no regularization is introduced and $f_\gamma^I = \overline{f}/(f\overline{f}) = 1/f$ reduces to the trivial inverse filter that is undefined whenever $f = 0$. However, for $\gamma > 0$, the denominator in equation (37) is always nonzero as it is the sum of two positive numbers, with γ controlling the maximum amplification of the spectrum at the singularities. While this addresses both the indeterminacy of the inverse filter at spatial frequencies where f is zero and the overamplification near those frequencies, there is a tendency to produce overregularized solutions. This happens because, in effect, we assume a constant SNR over the whole frequency spectrum. Thus, the amount of regularization introduced is essentially uniform in spatial frequency and ultimately determined by the smaller SNRs. This problem can be ameliorated by making use of a more realistic model for s_{mm}. Such a model should be flexible enough to reproduce different spectral decays of the magnetization PSD while being simple and having a minimum number of parameters. For instance, we may assume that the magnetization autocorrelation function R_{mm} is of the exponential form [*Jain*, 1989]

$$R_{mm}(x, y) = \rho^2 e^{-\rho\sqrt{x^2+y^2}}, \quad (38)$$

where ρ is a positive constant. The PSD—which is also circularly symmetric—is given by the zeroth-order Hankel transform of equation (38):

$$s_{mm}(\kappa) = \frac{\rho^3}{(\kappa^2 + \rho^2)^{3/2}}. \quad (39)$$

[53] Clearly, the PSD in equation (39) decays with frequency (ρ controls the rate of decay), which is a more realistic scenario, particularly for magnetization distributions of finite dimensions. In this case, the Wiener filter assumes the form

$$f_{\gamma,\rho}^I(\kappa_x, \kappa_y) = \psi_W(\kappa_x, \kappa_y) = \frac{\overline{f}(\kappa_x, \kappa_y)}{|f(\kappa_x, \kappa_y)|^2 + \gamma \frac{(\kappa^2+\rho^2)^{3/2}}{\rho^3}}, \quad (40)$$

which is equivalent to a constant magnetization PSD and a noise PSD that increases with frequency as the reciprocal of equation (39). The function ψ_W denotes the particular form of Wiener regularization utilized in this work to process synthetic and experimental data. The regularization of the inverse problem is governed by two parameters in this approach: γ adjusts the white-noise level, and ρ controls the

decay of the magnetization PSD. For our instrument and associated experimental conditions at MIT (double-layer shielded room with active compensation, low-T_c SQUID sensors, and high-precision nonmagnetic X-Y scanning stage), spatially white noise is an acceptable model for the noise found in the recorded field maps. However, other magnetic sensors or experimental setups may require careful modeling of different noise components, as well as separation of their characteristics along the scanning and transverse directions.

[54] Notice that, for practical purposes, this model incorporates equation (37) as a special case, given that $s_{mm} \to 1$ as $\rho \to \infty$. [Strictly speaking, equation (39) with very large ρ only approaches a constant function if $\kappa << \rho$. While this condition cannot be met in the continuous domain, as κ can be arbitrarily large, the equivalence will hold once we discretize the inverse problem and κ becomes bounded above by the Nyquist frequency (the reciprocal of twice the step size)]. Figure 3B summarizes the main steps of the inversion procedure.

2.4.2. Split Regularization

[55] Because direct inversion of equation (25) blows up due to two different reasons, it can be advantageous to introduce separate regularization schemes for the downward continuation and inverse directional derivative operators. Let us first regularize the downward continuation operator, which is the inverse of the upward continuation operator. [As we mentioned in section 2.3, the upward continuation operator is invertible given that it is a bijection (i.e., a one-to-one correspondence)]. This operator exhibits circular symmetry and grows without bounds.

$$f_{dwn}(\kappa_x, \kappa_y) = e^{h\sqrt{\kappa_x^2+\kappa_y^2}}. \quad (41)$$

[56] In this regularization scheme, we essentially wish to tame exponential growth past a cutoff frequency κ_0. There are several options to achieve this goal, but we favor the following scaling function, which allows for fine control of the regularized operator

$$q(\kappa) = 1 - \frac{1}{1 + e^{-\xi h(\kappa-\kappa_0)}} = \frac{e^{-\xi h(\kappa-\kappa_0)}}{1 + e^{-\xi h(\kappa-\kappa_0)}}, \quad (42)$$

where $\xi > 0$ determines the attenuation of the exponential term past κ_0. Thus, the regularized downward continuation operator is given by

$$\widetilde{f}_{dwn}(\kappa_x, \kappa_y) = \psi_{S1}(\kappa_x, \kappa_y) = C_0 \frac{e^{(1-\xi)h(\kappa-\kappa_0)}}{1 + e^{-\xi h(\kappa-\kappa_0)}}, \quad (43)$$

where $C_0 = e^{\kappa_0 h}$ is a constant and ψ_{S1} denotes the first function in the split regularization scheme utilized in the inversion of synthetic and experimental data in this paper.

[57] The effect of ξ on the regularized term is illustrated in Figure 4A. For $\xi < 1$, the function grows without bounds—but less rapidly than $e^{h\kappa}$—whereas for $\xi = 1$, the regularized term flattens out past a spatial frequency $\approx 1.5\kappa_0$. For $\xi > 1$, the function decays for frequencies above $\approx \kappa_0$, and the rate of decay is determined by the magnitude of ξ. Large values of ξ (>100) yield very sharp transitions, whereas values closer to unity produce a wider transition region. Large values of ξ also make the regularized term
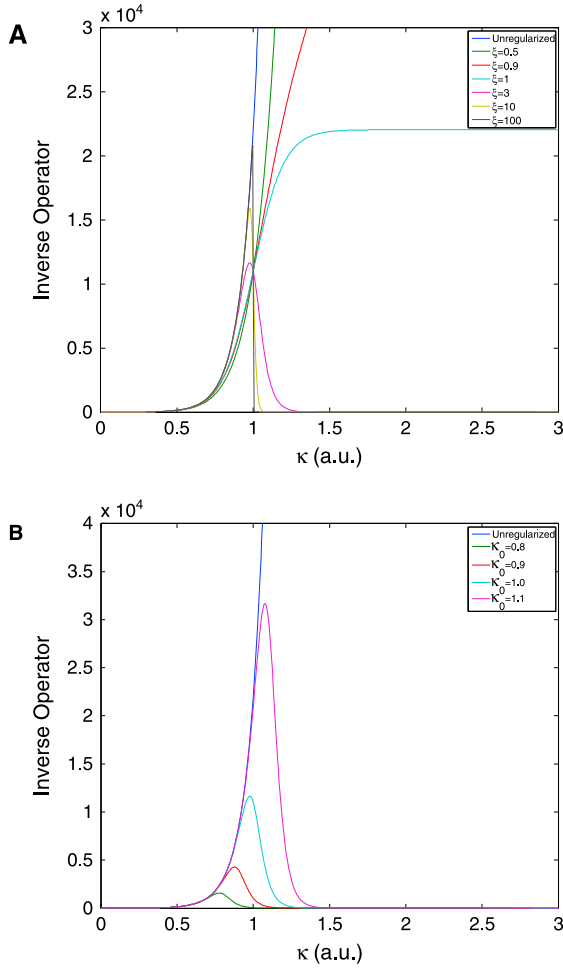
Figure 4. Regularization of the downward continuation operator (i.e., inverse upward continuation operator) used in the split regularization scheme. (a) Effect of the parameter ξ on the regularized operator ($\kappa_0 = 10$). (b) Effect of the parameter κ_0 on the regularized operator ($\xi = 3$).

closely track the exponential $e^{h\kappa}$ up to the vicinity of κ_0. Even though this is a desirable property, sharp transitions might lead to ringing artifacts in the solution. Typically, ξ ranges between 1 and 20, where the optimal value depends on the noise level as well as the size of the mapping area. The effect of κ_0 on the regularized downward operator is shown in Figure 4B. It essentially controls the location of the transition between tracking of the exponential and attenuation.

[58] Inverting the directional derivative operator is more complicated, given that the mapping is not a one-to-one correspondence and an inverse does not strictly exist. In this case, we use the parametric Wiener deconvolution approach previously described to regularize the inverse operator. Notice that for magnetizations that are not purely in-plane, the inverse directional derivative operator is only ill defined near the origin of the spatial frequency plane, and most of the overall regularization is associated with the downward continuation operator. For those cases, which constitute the vast majority of unidirectional magnetizations found in practice, a simpler Wiener filter like equation (37) is often sufficient to regularize the inverse directional derivative

operator, thereby helping reduce the total number of regularization parameters. In particular, we utilized the following regularized operator for the inversion of the directional derivative operator (including the scaling factor):

$$\psi_{S2}\left(\kappa_x, \kappa_y\right) = \frac{\overline{f}_D\left(\kappa_x, \kappa_y\right)}{\left|f_D\left(\kappa_x, \kappa_y\right)\right|^2 + \gamma'}, \qquad (44)$$

where $\quad f_D\left(\kappa_x, \kappa_y\right) = -\frac{\mu_0}{2}\left[\ \left(i\kappa_x\right)\sin\theta\cos\varphi + \left(i\kappa_y\right)\sin\theta\right.$ $\sin\varphi - (\kappa)\cos\theta]$, and ψ_{S2} is the second function in the split regularization scheme used for processing synthetic and experimental data in this work.

2.5. Discretization of the Inverse Problem

[59] The equations described so far are all in the continuous domain, and proper discretization of the inverse problem is critical for attaining adequate accuracy when inverting experimental data. The key point is realizing that equations such as equation (25) and regularized versions of equation (33) express relationships between *continuous* Fourier transforms of the field and magnetization, which are not available to us in practice. We must instead estimate these quantities from discrete measurements of the magnetic field by means of approximate equations calculated only in a section of the spatial frequency plane. The mere discretization of such equations is frequently not sufficient for obtaining high-quality inversions, and solutions may be severely contaminated by artifacts even in the ideal case where data are noise free.

[60] A number of factors impact the quality of estimated magnetization distributions; we present in Appendices A and B a detailed analysis of discretization as well as a discussion of practical issues that affect accuracy in the inversion process. We stress that discretization should not be overlooked, and that addressing those issues is critical to obtaining high-quality inversions. We summarize below the main results of our discretization and accuracy analyses.

2.6. Summary

[61] We have shown in section 2 and Appendices A and B that:

[62] 1. The inverse problem for scanning magnetic microscopy is, in general, nonunique. In particular, the inversion of in-plane (horizontal) unidirectional magnetizations with infinite (unbounded) support is nonunique because distributions that are constant along the magnetization direction but varying in the transverse direction may be added to the solution without changing the observed field. However, inversion of unidirectional magnetization distributions with finite dimensions—the geometry encountered in magnetic microscopy applications—is unique irrespective of the magnetization direction.

[63] 2. Expressing the inverse problem in the Fourier domain implicitly incorporates magnetization distributions with infinite support into the modeling, owing to the transformation of integral equation (1) into a two-dimensional convolution.

[64] 3. Calculating inversions exclusively from field components parallel to the sample plane provides intrinsically less accurate estimates of the magnetization than inversions based on the field component normal to the sample plane, as
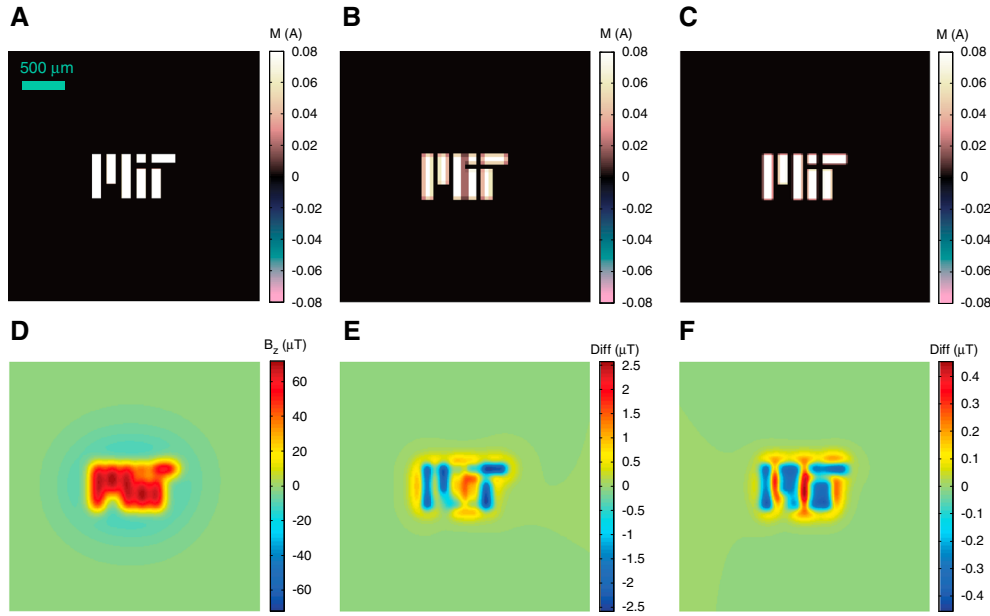
Figure 5. Magnetization intensity images of the primary test distribution in the shape of the MIT logo and of its two discretized versions. All distributions were magnetized in the +z direction ($\theta = 0°$). (a) No discretization (slabs). (b) Discretization obtained with an array of 64×64 square source elements distributed over the mapping area. (c) Discretization obtained with an array of 128×128 square source elements distributed over the mapping area. (d) Z component of the magnetic field produced by the primary test distribution shown in Figure 5A. (e) Difference between the field map produced by the discretized distribution shown in Figure 5B and the primary field map shown in Figure 5D. (f) Difference between the field map produced by the discretized distribution shown in Figure 5C and the primary field map shown in Figure 5D. (Each image corresponds to an area of $2.8 \times 2.8 \, \text{mm}^2$. Field maps were calculated $150 \, \mu\text{m}$ above the sample).

in this case there is a larger region in the spectrum where the inversion cannot be directly computed.

[65] 4. A unidirectional magnetization distribution whose direction does not lie in the plane of the sample may be estimated—up to a constant—from the field component normal to the magnetization plane.

[66] 5. In-plane unidirectional magnetization estimates may exhibit inaccuracies and distortions, particularly in the form of undulations perpendicular to the magnetization direction.

[67] 6. Regularization must be introduced to define the inverse operator near singularities and to limit excessive amplification of noise and spectral artifacts. We found that both parametric Wiener deconvolution and split regularization methods yielded good results.

[68] 7. Finite mapping areas create undulations in the spectrum that might be magnified by the inverse filter—even in the noiseless case—leading to ripples in the spatial domain that could easily dominate a solution obtained without proper regularization.

[69] 8. Finite sensor effective areas/volumes may often negatively impact inversion accuracy if not properly modeled. These effects are usually undone by solving an ancillary inverse problem prior to computing the solution to the inverse problem for magnetizations.

3. Results and Discussion

[70] To test our technique, we performed inversions on simulated magnetization distributions, synthetic samples,

and representative geological samples. In all examples, we did not make use of any prior knowledge of the sample's characteristics to adjust the regularization. Instead, the procedure described in section 3.2.1 was always followed to heuristically obtain the optimal parameter values in either equation (40) or equations (43)–(44). In particular, simulated and synthetic samples were treated as if their magnetization distributions were completely unknown for the purposes of tuning the regularization. Of course, to compute the error in the reconstruction, it is necessary to know what the true magnetization distribution is, which is only possible for simulated distributions. We also describe in section 3.2.1 a method to estimate the magnetization direction. For synthetic and geological samples, bulk moment magnetometry provided initial estimates for the direction of the magnetization and for its average strength (net moment). Specific regularization parameter values for the inversions shown in this section are available in Appendix C. Notice, however, that those values are useful for comparison purposes only, given that different experimental setups, mapping areas, sensor noise levels, mapping step sizes, and sensor-to-sample distances may greatly impact the choice of regularization parameters.

3.1. Simulated Test Sources

[71] We devised several simulated sources and calculated their magnetic field maps to evaluate our technique. This allowed us to test the technique in a controlled experiment and to characterize its behavior under challenging conditions that would only rarely occur in practice, such as discontinuous
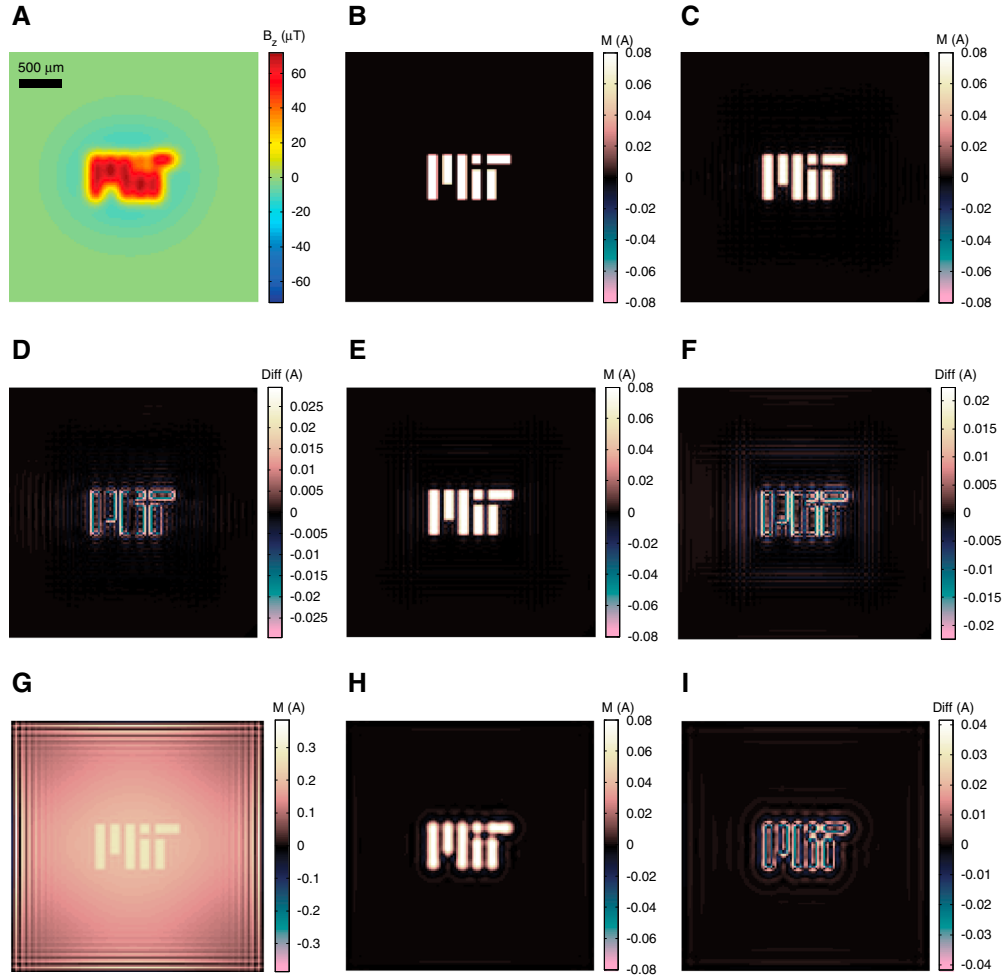
Figure 6. Inversion of the field map produced by the primary test magnetization distribution in the shape of the MIT logo (piecewise continuous) calculated using different regularization schemes. (a) Simulated z component field map of the primary distribution shown in Figure 5A (magnetized in the $+z$ direction). The map was measured on a 128×128 square grid of positions $150\,\mu m$ above the sample. (b) Target magnetization distribution with 128×128 elements, matching the discretization parameters of the field map. (c) Inversion of the field map shown in Figure 6A using split regularization together with pre- and postwindowing. (d) Difference between the recovered magnetization shown in Figure 6C and the target magnetization shown in Figure 6B. (e) Inversion of the field map shown in Figure 6A using Wiener deconvolution together with prewindowing. (f) Difference between the recovered magnetization shown in Figure 6E and the target magnetization shown in Figure 6B. (g) Inversion of the field map shown in Figure 6A using Wiener deconvolution with the same parameters as in Figure 6E but without prewindowing. Notice that artifacts due to limited mapping area dominate the solution. (h) Inversion of the field map shown in Figure 6A using Wiener deconvolution again without prewindowing but now with regularization parameters adjusted to tame artifacts. Notice that the spatial resolution of the solution is severely impacted, resulting in rounded edges around the slabs (compare with Figures 6C and 6E). (i) Difference between the recovered magnetization shown in Figure 6H and the target magnetization shown in Figure 6B. The error in the recovery is almost twice larger (compare with Figures 6D and 6F). Each image corresponds to an area of $2.8 \times 2.8\,\text{mm}^2$. Magnetization distributions in Figures 6C, 6E, and 6H are shown in the same color scale as Figure 6B to facilitate comparison.

boundaries and severe noise contamination. By showing that the inversion technique still performs reasonably well even in those adverse cases, we demonstrate its robustness and reveal its limitations.

[72] The magnetization distribution that served as the foundation for all simulations used in this work consisted of uniformly magnetized slabs with infinitesimal thickness arranged in the shape of the Massachusetts Institute of Technology (MIT)'s logo (Figure 5A). (All slab dimensions are multiples of a fundamental size given by the $100 \times 100\,\mu m^2$ square slab that represents the dot over the letter "I." In addition, all slabs have the same magnetization of 0.08 A. Because the distribution is two dimensional, the magnetization unit is A instead of A/m. If one assumed that this was a model for a real three-dimensional sample with $30\,\mu m$ thickness, the corresponding magnetization would
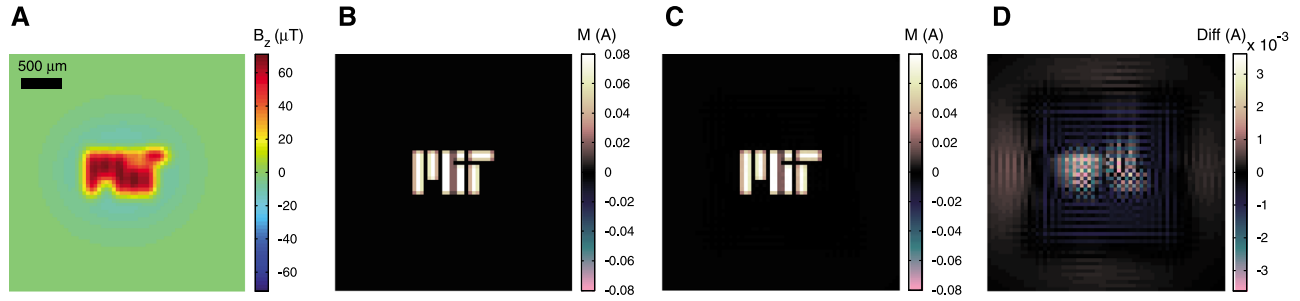
Figure 7. Inversion of the field map produced by a 64×64 discretized test magnetization distribution in the shape of the MIT logo. (a) Simulated z component field map of the test distribution shown in Figure 7B magnetized in the $+z$ direction. The map was measured on a 64×64 square grid of positions 150 μm above the sample. (b) Target magnetization distribution with 64×64 elements. (c) Inversion obtained with Wiener deconvolution together with prewindowing. (d) Difference between the recovered magnetization shown in Figure 7C and the target magnetization shown in Figure 7B. Notice the substantial improvement in recovery error owing to the absence of discretization effects.

be 2667 A/m.) In one case, field maps were calculated directly from this primary magnetization by means of analytical formulas [*Talwani*, 1965] to test inversions of piecewise-continuous distributions. For the remaining simulated test sources, this primary magnetization was discretized using either a 64×64 grid or a 128×128 grid of square source elements evenly distributed over a $2.8 \times 2.8 \, mm^2$ area (Figures 5B and 5C, respectively).

[73] For the discretized test sources, each square source element ($22.0 \times 22.0 \, \mu m^2$ and $44.4 \times 44.4 \, \mu m^2$ for the fine and coarse grids, respectively) was represented by a single magnetic dipole, which is an adequate model for a liftoff several times
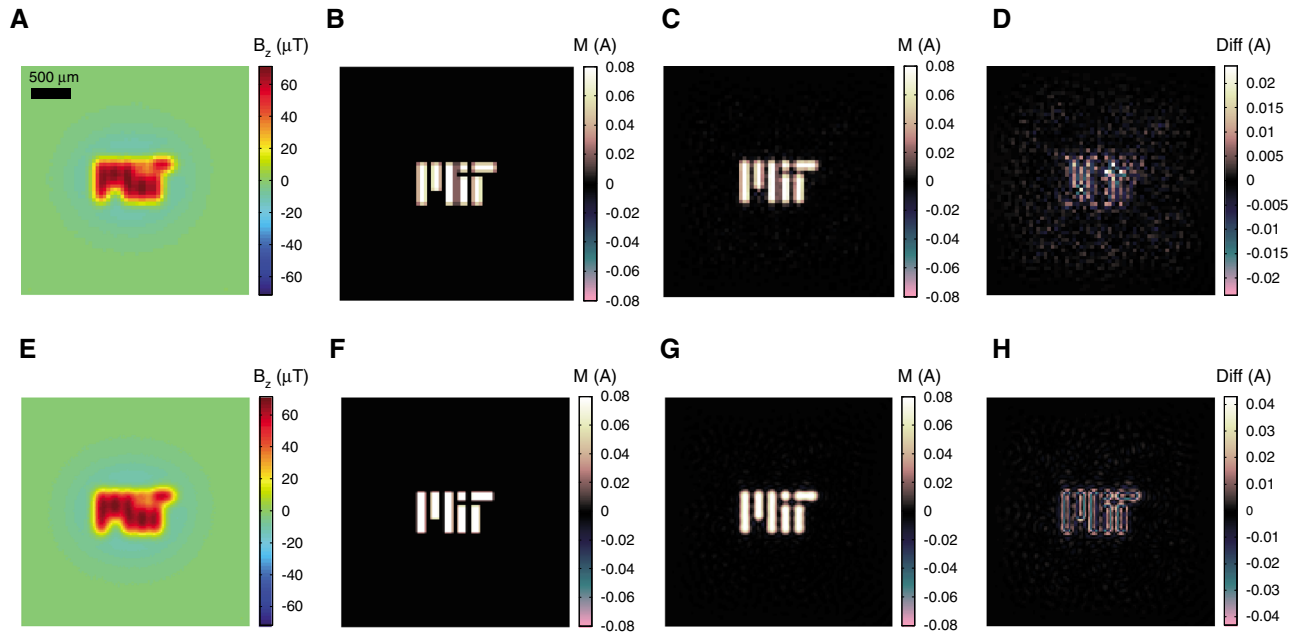

Figure 8. Inversion of the field maps produced by 64×64 and 128×128 discretized test magnetization distributions in the shape of the MIT logo. The z component field maps were corrupted by Gaussian white noise such that the signal-to-noise ratio was 40 dB. (a) Simulated z component field map of the test distribution shown in Figure 8B magnetized in the $+z$ direction. The map was measured on a 64×64 square grid of positions 150 μm above the sample. (b) Target magnetization distribution with 64×64 elements. (c) Inversion obtained with Wiener deconvolution together with prewindowing. (d) Difference between the recovered magnetization shown in Figure 8C and the target magnetization shown in Figure 8B. (e) Simulated z component field map of the test distribution shown in Figure 8F magnetized in the $+z$ direction. The map was measured on a 128×128 square grid of positions 150 μm above the sample. (f) Target magnetization distribution with 128×128 elements. (g) Inversion obtained with Wiener deconvolution together with prewindowing. (h) Difference between the recovered magnetization shown in Figure 8G and the target magnetization shown in Figure 8F. Magnetizations in Figures 8B, 8C, and in 8F, 8G are shown in the same color scale to facilitate comparison.
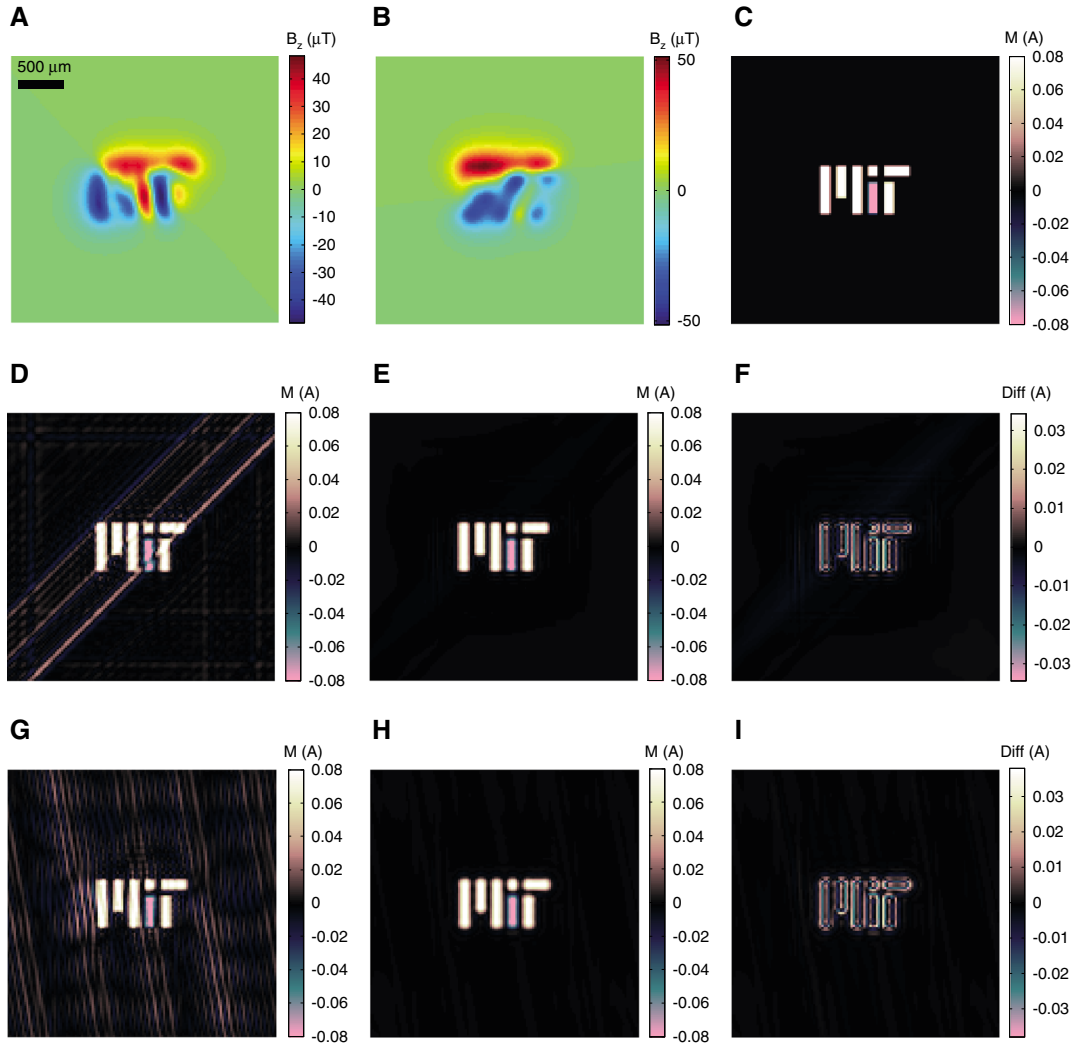
Figure 9. Inversion of field maps produced by the primary test magnetization distribution in the shape of the MIT logo (piecewise continuous) when magnetized in directions lying in the horizontal plane. (a) Simulated z component field map of the primary distribution shown in Figure 5A magnetized in the directions ($\theta = 90°$, $\varphi = 45°$) and ($\theta = 90°$, $\varphi = 225°$). The map was measured on a 128×128 square grid of positions $150\,\mu m$ above the sample. (b) Simulated z component field map of the primary distribution shown in Figure 5A magnetized in the directions ($\theta = 90°$, $\varphi = 100°$) and ($\theta = 90°$, $\varphi = 280°$). The map was measured on a 128×128 square grid of positions $150\,\mu m$ above the sample. (c) Target magnetization distribution with 128×128 elements, matching the discretization parameters of the two field maps. (d) Inversion of the field map shown in Figure 9A using split regularization together with prewindowing. Notice the silent-source artifacts superimposed to the physical solution corresponding to lines of constant strength parallel to the magnetization direction. (e) Inversion of the field map shown in Figure 9A using increased split regularization to greatly reduce artifacts while still achieving adequate spatial resolution. (f) Difference between the recovered magnetization shown in Figure 9E and the target magnetization shown in Figure 9C. (g) Inversion of the field map shown in Figure 9B using split regularization together with prewindowing. Notice the silent-source artifacts superimposed to the physical solution corresponding to lines of constant strength parallel to the magnetization direction. (h) Inversion of the field map shown in Figure 9B using increased split regularization to greatly reduce artifacts while still achieving adequate spatial resolution. (i) Difference between the recovered magnetization shown in Figure 9H and the target magnetization shown in Figure 9C. Magnetization distributions in Figures 9C, 9D, 9E, 9G, and 9H are shown in the same color scale to facilitate comparison.

larger than the size of the element. Because the same type of source distribution was used both in the simulation and in the modeled solution, this reduced discretization effects and provided smoother boundaries, allowing for artifacts in the solution caused by the inversion process to be isolated from those originating from discretization issues. The dipole strength was scaled proportionally to the area of the corresponding source element lying inside the nearest magnetization slab in the primary test distribution. Thus, if a source element lay completely inside of a slab, the dipole strength was 100%

of the magnetization intensity times the area of the element. If, on the other hand, only 50% of the element lay inside the slab, for instance, the dipole strength was half that value.

[74] Our first set of inversions (Figures 6–9 and S2–S4) focused on vertically magnetized unidirectional magnetization distributions with finite support. As discussed above, we should be able to uniquely retrieve these magnetizations from z component field data. The two discretized distributions (Figures 5B and 5C) are considered the target distributions (that is, the benchmarks for the inversions of our simulated test sources), because they are merely discretized versions of the piecewise-continuous primary magnetization distribution. Clearly, they are not attainable in practice if one were to invert field maps associated with the primary test distribution. This is a direct consequence of the Wiener deconvolution formulation, given that the strength of the discretized magnetization is always smaller than or equal to that of the nondiscretized one. The equality would only hold if the discretization was such that every planar source element lay fully inside or fully outside of a slab. Therefore, they cannot be the solutions that minimize the MSE between the recovered and the true magnetizations, even in the ideal case where the PSD of the true magnetization is known beforehand and noise is absent. This is because a minimum MSE solution cannot be everywhere smaller than the true magnetization, given that it would violate the error minimization condition. (Similarly, a least squares best fit line will never lie below or above all data points.) Interestingly, their field maps are not the closest ones (in the least squares sense) to the field map associated with the primary distribution either. This is evident from Figures 5D–5F, which present the field maps produced by the primary test magnetization distribution and the discrepancies between this field map and those associated with the two discretized test distributions. As expected, the finer the discretization, the smaller the difference between the field maps of the discretized and nondiscretized distributions.

[75] Therefore, if the criterion consisted of minimizing the MSE between model and experimental *field maps*—as usually is the case in spatial-domain inversion techniques—the discretized distributions would not be the solutions yielding the smallest residuals. Nevertheless, these target distributions are fairly close to the best mathematical solutions in the least squares sense and are, in fact, the expected physical ones.

[76] All examples in this section were calculated for a fixed liftoff $h = 150\,\mu m$, which is a representative liftoff in scanning magnetic microscopy. As discussed in Appendix A, this value by itself is unimportant: the critical quantity is the ratio of the step size to the liftoff (if we scale both the liftoff and the step size by a factor C, the discretized inverse problem remains unchanged). We utilized the normalized root-mean square deviation (NRMSD) to numerically quantify the discrepancies between the recovered and true magnetizations:

$$\text{NRMSD} = \left[\frac{\int\limits_{-\infty}^{+\infty} \int\limits_{-\infty}^{+\infty} \left| \hat{M}(x,y) - M(x,y) \right|^2 dxdy}{\int\limits_{-\infty}^{+\infty} \int\limits_{-\infty}^{+\infty} \left| M(x,y) \right|^2 dxdy} \right]^{1/2}, \quad (45)$$

where $\hat{M}$ and M stand for the recovered and true magnetization

distributions, respectively. We also computed the difference between the two magnetizations, which reveals the spatial distribution of the error and the degree to which it is spatially correlated.

[77] The SNR is used to quantify the amount of signal degradation in the presence of noise, being usually expressed in decibels (dB):

$$\text{SNR} = 10 \log_{10} \left(\sigma_{signal}^2 / \sigma_{noise}^2 \right), \quad (46)$$

where σ_{signal}^2 is the variance of the (noiseless) field map, and σ_{noise}^2 is the variance of the noise. In some of our examples, we used additive Gaussian white noise to simulate sensor noise. We assume that measurements are performed inside a shielded chamber, so that environmental noise can be considered negligible. Notice, however, that other experimental configurations using different sensors and scanning stages may require revised sensor and environmental noise models to better reflect their spectral characteristics. In addition, signal-dependent noise may also have to be taken in account depending on the degree of imprecision in positioning the sample.

[78] We compared different regularization schemes for inversions of primary test distribution field data (Figure 6). Although the true magnetization distribution is (piecewise) continuous in this case, both the field map and the source model must necessarily be discretized in order to produce finite amounts of data. As in all examples in this paper, the magnetization model and field map discretizations are identical, meaning that each source element shares the same horizontal (x,y) coordinates with a corresponding magnetic field measurement. Depending on the case, this discretization may or may not coincide with the discretization of the simulated magnetization distribution (if applicable). In this example, the simulated z component magnetic field map (Figure 6A) was calculated on a 128×128 square grid of positions $150\,\mu m$ above the test magnetization shown in Figure 5A, which was magnetized in the $+z$ direction ($\theta = 0°$). The 128×128 discretized target magnetization (intensity map) is shown in Figure 6B. We first computed an inversion using the split regularization scheme with Tukey prewindowing (see Appendix A), which is shown in Figure 6C. Figure 6D displays the difference between this estimated magnetization distribution and the target magnetization distribution (Figure 6B), corresponding to an NRMSD of 0.11. Notice that most of the discrepancies are located predominantly at the edges of the slabs. This behavior is expected because discontinuities require very high frequencies to be properly represented in the Fourier domain, which is not attainable once the inverse problem is discretized and regularization is introduced to tame noise amplification. As a consequence, sharp edges are often not well represented in recovered magnetizations leading to localized increases in the recovery error. The dissimilarities seen in the recovered magnetization originate from three main sources (see Figure 5 and Appendix A): (i) differences in the field maps produced by the simulated sources (piecewise continuous) and model source distribution (discretized), (ii) artifacts due to limited mapping areas, and (iii) the maximum spatial frequency for which the deconvolution is calculated, which is determined by the field map step size.

[79] Next, we calculated an inversion of the same field map using Wiener regularization with Tukey prewindowing (Figure 6E). Figure 6F displays the difference between this recovered magnetization and the target magnetization shown in Figure 6B, corresponding to an NRMSD of 0.10. In this specific case, use of the Wiener regularization yielded slightly better results. To illustrate how prewindowing can greatly aid in taming mapping area artifacts while yielding higher spatial resolution estimates for the underlying magnetization distributions, we also computed the inversion using Wiener deconvolution with the very same parameters employed in the inversion shown in Figure 6E but without prewindowing (Figure 6G). It is clear that the solution is dominated by artifacts far exceeding the strength of the primary magnetization. To reduce such artifacts, we have to increase the degree of regularization (Figure 6H). While such a solution is still acceptable, it has much lower spatial resolution than those obtained with prewindowing (cf. Figures 6C and 6E). The difference between this solution and the target magnetization shown in Figure 6B is larger than with prewindowing (NRMSD = 0.16) (Figure 6I). Notice that, as expected, there is a significant increase in the recovery error. Comparable results for the primary test distribution were obtained when using a 64×64 discretized field map instead (Fig. S2 in supporting information).

[80] To distinguish discretization effects from other sources of inaccuracy, we computed inversions of field maps generated by the target magnetization distributions rather than by the primary distribution. In this case, the simulated sources and model sources have the same discretization. Figure 7A shows the simulated z component magnetic field map produced by the 64×64 target magnetization displayed in Figure 7B. The target distribution was magnetized in the $+z$ direction, and the field map was computed on a 64×64 grid of positions 150 μm above the sources. Figure 7C shows the inversion obtained with Wiener deconvolution and Tukey prewindowing, while Figure 7D shows the difference between this solution and the target magnetization (Figure 7B), which corresponds to an NRMSD of 0.05. Notice that both the discrepancies and the NRMSD dropped sharply in this case (compare Figures 7D and S2D). Intriguingly, such an improvement could not be achieved for the 128×128 test magnetization distribution (Fig. S3). The reason for this lies in the extended spatial frequency range where the deconvolution is calculated for the latter. It clearly illustrates that the limiting factor here is linked to mapping area artifacts. In particular, undulations in the spectrum of the magnetic field map caused by a limited mapping area require an increased degree of regularization at higher spatial frequencies to avoid excessive magnification by the inverse operator, unlike for the 64×64 case where accuracy was mostly impacted by discretization issues. Whereas this may seem surprising at first, one cannot expect to improve spatial resolution without trading off accuracy.

[81] We then analyzed the effects of noise contamination in the field maps on the recovery quality. Here, we also utilized discretized simulated sources in the inversions to again decouple discretization effects from noise effects. Figure 8A shows a 64×64 z component field map simulated 150 μm above the 64×64 test distribution (Figure 8B), which

was again magnetized in the $+z$ direction. The field map was corrupted by white noise so as to yield a SNR of 40 dB, and the inversion was obtained with Wiener deconvolution and Tukey prewindowing (Figure 8C). The difference between this inversion and the target magnetization is displayed in Figure 8D (NRMSD = 0.22). Notice that the error in the recovery is similar to the one achieved with the primary test distribution with noiseless data (cf. Fig. S2).

[82] Increasing the resolution of the field map and corresponding model source discretization resulted in an increase in recovery error and decrease in spatial resolution compared to the noiseless case. A 128×128 z component field map was simulated 150 μm above the 128×128 test magnetization shown in Figure 8F and corrupted by white noise (SNR = 40 dB) (Figure 8E). The test distribution was magnetized in the $+z$ direction. The inversion was calculated using Wiener deconvolution and prewindowing (Figure 8G). Figure 8H shows the difference between the recovered and test magnetizations, which corresponds to an NRMSD of 0.15. Given that the deconvolution is computed to higher spatial frequencies, additional regularization is required to prevent excessive noise amplification, thereby impacting spatial resolution and accuracy (compare Figure 8G with Figures 6C and 6E). We repeated these tests under very low SNRs to determine whether it was still possible to recover meaningful information in such adverse conditions. Figure S4 shows the inversion results for an SNR of just 10 dB. While it is not possible to completely filter out noise in the solution without drastically sacrificing spatial resolution, the results demonstrate that the technique is, in fact, quite robust.

[83] Our second set of inversions focused on the reconstruction of in-plane magnetizations, which as discussed above are likely to be limited by the presence of magnetically silent sources superimposed to inversions. We carried out these inversions using unidimensional distributions (i.e., dual-polarity unidirectional magnetizations that effectively correspond to two antipodal magnetization directions) to demonstrate the performance of the technique for this broader category of magnetizations patterns. We utilized a modified version of the primary test distribution, in which the main part of the letter "I" is magnetized in the antipodal direction, to generate the magnetic field maps. A 128×128 z component field map was simulated at a liftoff of 150 μm, corresponding to the modified primary test distribution magnetized in the horizontal plane along the directions ($\theta = 90°$, $\varphi = 45°$) and ($\theta = 90°$, $\varphi = 225°$) (Figure 9A). A second 128×128 z component field map was simulated at a liftoff of 150 μm, corresponding to the modified primary test distribution also magnetized in the horizontal plane but along different directions: ($\theta = 90°$, $\varphi = 100°$) and ($\theta = 90°$, $\varphi = 280°$). The 128×128 target distribution is shown in Figure 9C, while inversion of the data shown in Figure 9A obtained with split regularization and (soft) Tukey prewindowing is displayed in Figure 9D. Notice the streaks along the magnetization direction associated with silent sources superimposed on the solution (NRMSD =0.30) (see section 2.2). Increasing the regularization helps reduce such artifacts while still achieving a good spatial resolution (Figure 9E). Figure 9F displays the difference between the inversion shown in Figure 9E and the target magnetization shown in Figure 9C, corresponding to an NRMSD of 0.13. The inversion for the second set of

magnetization directions was also obtained with split regularization and (soft) Tukey prewindowing (Figure 9G). Notice that the streaks associated with silent sources appear again oriented along the magnetization directions (NRMSD = 0.36). The inversion obtained with enhanced regularization is mostly free of artifacts (Figure 9H). Figure 9I displays the difference between the inversion shown in Figure 9H and the target magnetization shown in Figure 9C, corresponding to an NRMSD of 0.14. Upon close inspection of Figures 9D and 9G, we can see that the streaks are not perfectly constant throughout their lengths. This phenomenon is due to the concurrent effect of having finite mapping areas, which tends to introduce undulations in the solution.

3.2. Synthetic Samples

[84] We proceeded to test our technique on real experimental magnetic field data taken on controlled, synthetic samples. The samples were toner particles deposited on a sheet of paper in different geometric configurations using a laser printer. The pieces of printed paper were magnetized and then taped to 1 inch nonmagnetic quartz discs, which were subsequently scanned with our SQUID microscope instrument in the MIT Paleomagnetism laboratory shielded room (ambient field <40 nT). To test more complicated patterns that are still easily recognizable, we printed the logos of the three institutions involved in this research: the MIT, Vanderbilt University (VU), and the Institut National de Recherche en Informatique et en Automatique (INRIA). Each synthetic sample was magnetized in a different way by imparting either one or two strong-field isothermal remanent magnetization (IRM) patterns, as described below. When the direction(s) of the magnetization distribution could not be estimated with confidence prior to performing an inversion, we utilized a commercial superconducting rock magnetometer (2G Enterprises, model 755) to measure the net moment of either whole synthetic samples (unidirectional and unidimensional patterns) or their constituent pieces prior to assemblage (bidirectional patterns).

3.2.1. Unidirectional Case—Finding the Magnetization Direction and Adjusting the Regularization Parameters

[85] We began by magnetizing the VU logo synthetic sample into the plane (i.e., −z direction) (Figure 10A). We mapped the z component of the magnetic field 280 μm above the sample (Figure 10B). We then calculated inversions for the measured field map using three different degrees of regularization of the Wiener deconvolution, aiming to exemplify how the regularization parameters are heuristically adjusted in practice, particularly when the target magnetization is not known.

[86] In this case, we have an accurate estimate for the magnetization direction because we imparted a laboratory magnetization in a fixed known direction and the sample does not exhibit magnetic anisotropy. However, suppose that such information was not known beforehand and that a bulk moment magnetometer was not readily available to provide an initial guess for the magnetization direction. We estimate the direction by uniformly tiling a unit sphere and, for each direction, computing an inversion (magnetization distribution). Special algorithms for distributing points on a sphere avoid the concentration of points around the poles and ensure uniform sampling of all possible directions

[*Saff and Kuijlaars*, 1997]. A practical criterion to find the magnetization direction consists of computing the size (L1 norm) of the negative part of the magnetization estimated for each direction:

$$I_N\left(\hat{M}_{\theta,\varphi}\right) = \int\int \max\left(-\hat{M}_{\theta,\varphi}(x,y), 0\right) dx\, dy, \qquad (47)$$

where $\hat{M}_{\theta,\varphi}$ stands for the magnetization recovered for the direction (θ, φ). The estimated magnetization direction is the one corresponding to the solution with the smallest negative part.

[87] Because our inversion technique is very fast, we illustrate this approach by tiling the sphere with a large number of cells. For each of the 600 directions, we compute the size of the negative part of the inversion of the magnetic field data shown in Figure 10B calculated in that particular direction. We then build a map of the size of the negative part as a function of magnetization direction, as shown in Figure 10C. Here, we first normalize the norm of the negative part by the value corresponding to the direction exhibiting the largest negative part—as only relative magnitude is relevant—and present the data in a log color scale to enhance visualization. It is clear that the direction with the smallest negative part corresponds to the actual magnetization direction −z.

[88] In practice, an initial guess for the magnetization direction is almost always available from bulk moment magnetometry, a priori knowledge about the sample, or qualitative analysis of the field maps. In this situation, we tile a section of the sphere around the estimated direction and compute the norm of the negative part only in that region. Besides saving time, this allows for finer sampling of directions. It is usually beneficial to "fine tune" the magnetization direction used in the inversion because the initial estimates may often be biased by background sources such as sample mounts and holders. Even in the case of nonunidirectional magnetization distributions, it is advisable to manually search around the initial guess for the direction that effectively minimizes streaking. The magnetization directions for all examples with experimental data shown in this paper were obtained following one of these two procedures, depending on whether the magnetization was unidirectional or unidimensional/multidimensional.

[89] Next, we examine the issue of adjusting the regularization parameters to find solutions with superior spatial resolution and accuracy with minimal occurrence of artifacts. The key point is realizing the trade-off present in equation (40) and in equations (43)–(44): increasing the regularization tames artifacts and noise magnification at the expense of spatial resolution and accuracy. Solutions that are overregularized usually look overly spatially smoothed. On the other hand, underregularized solutions typically appear unnaturally sharp and may exhibit peaking and ringing artifacts. Plotting the spatial frequency spectrum of the solutions as the parameters are changed is often very helpful to ascertain whether a particular solution is under- or overregularized.

[90] We illustrate this point by computing inversions of the field map shown in Figure 10B using different regularization parameters. The first inversion is clearly overregularized (Figure 10D), as it actually exhibits lower spatial resolution than the experimental magnetic field map. A plot of the
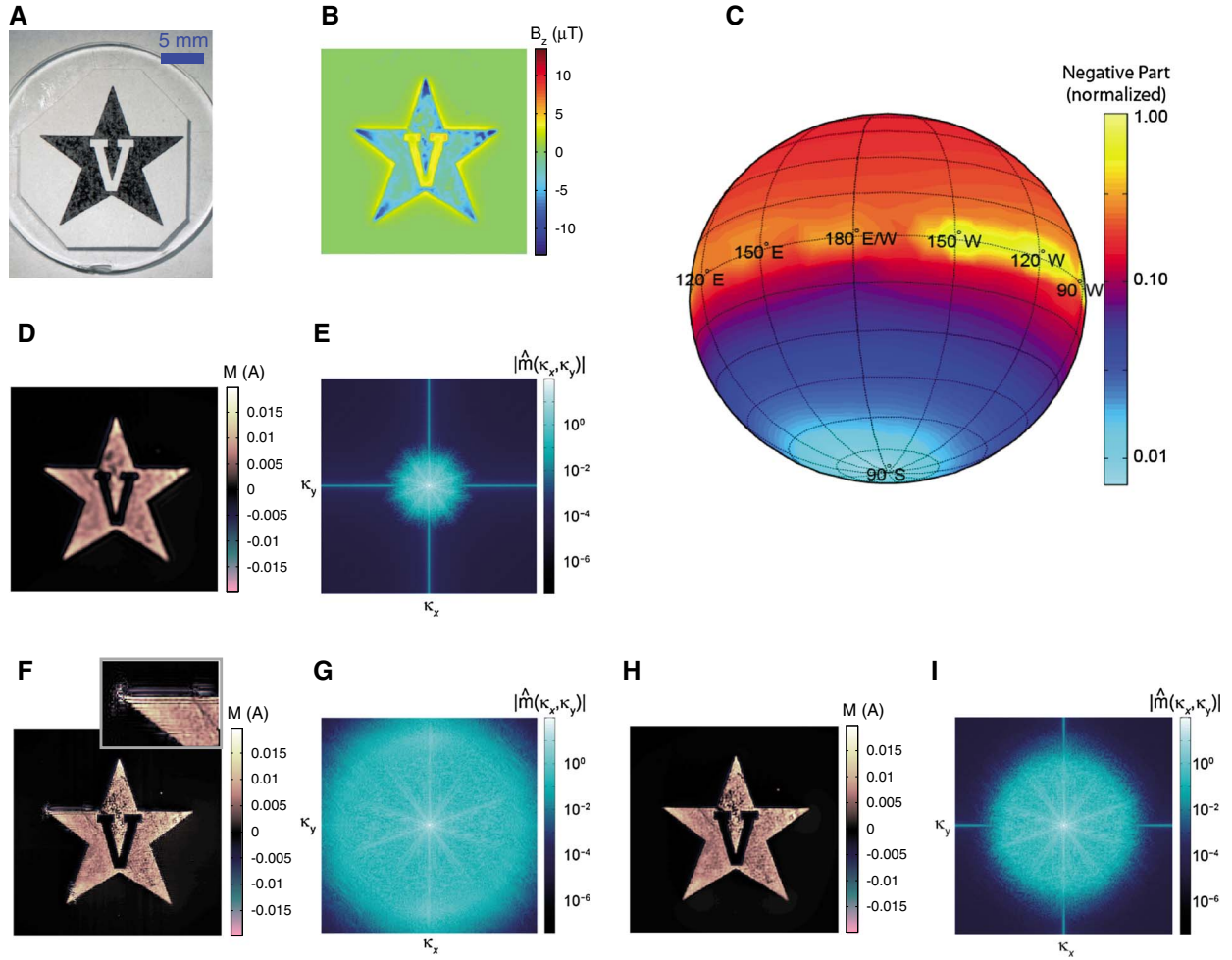
Figure 10. Inversion of experimental magnetic field data for a synthetic sample with unidirectional magnetization distribution. (a) Optical picture of synthetic sample consisting of VU's "V-Star" logo printed on a small piece of paper. A sIRM (900 mT peak field) was imparted in the $-z$ direction. (b) Z component field map of the sample shown in Figure 10A measured with our SQUID microscope. The map was measured on a 294×294 square grid of positions 280 μm above the sample with a step size of 75 μm. (c) Plot of the normalized size of the negative part of the recovered magnetization as a function of the magnetization direction used in the inverse model (log color scale). (d) Inversion of the field map shown in Figure 10B obtained with Wiener deconvolution together with prewindowing using an excessive degree of regularization. Notice that the recovered magnetization is "blurry," with an effective spatial resolution that is in fact lower than the one of the associated field map. (e) Plot of the magnitude of the two-dimensional Fourier transform of the magnetization distribution shown in Figure 10D (log color scale). Note that the frequency spectrum is almost exclusively comprised of low spatial frequencies, confirming the low spatial resolution observed in Figure 10D due to excessive regularization. (f) Inversion of the field map shown in Figure 10B obtained with Wiener deconvolution together with prewindowing using an insufficient degree of regularization. Notice that the recovered magnetization is unnaturally sharp, with visible artifacts around the two left-hand vertices of the star. Inset shows detailed view of the upper left-hand vertex of the star and the artifacts located in that region. (g) Plot of the magnitude of the two-dimensional Fourier transform of the magnetization distribution shown in Figure 10F (log color scale). In this case, the frequency spectrum contains an excess of high frequencies that extends to the upper and lower limits of the spatial frequency axes, which correspond to the maximal spatial frequencies that can be represented in the discrete domain for a given mapping step size. (h) Inversion of the field map shown in Figure 10B obtained with Wiener deconvolution together with prewindowing using an adequate degree of regularization. Notice that the recovered magnetization is fairly sharp but free of artifacts. (i) Plot of the magnitude of the two-dimensional Fourier transform of the magnetization distribution shown in Figure 10H (log color scale). Here, we observe an adequate amount of high-frequency spectral content with sufficient distance from the limits of the spatial frequency axes, which ensures superior spatial resolution without occurrence of noticeable artifacts in the solution. Magnetization distributions in Figures 10D, 10F, and 10H are shown in the same color scale to facilitate comparison. Spatial frequency axes in Figures 10E, 10G, and 10I range from $-\pi/\Delta$ to $+\pi/\Delta$, where $\Delta = 75$ μm is the mapping step size.
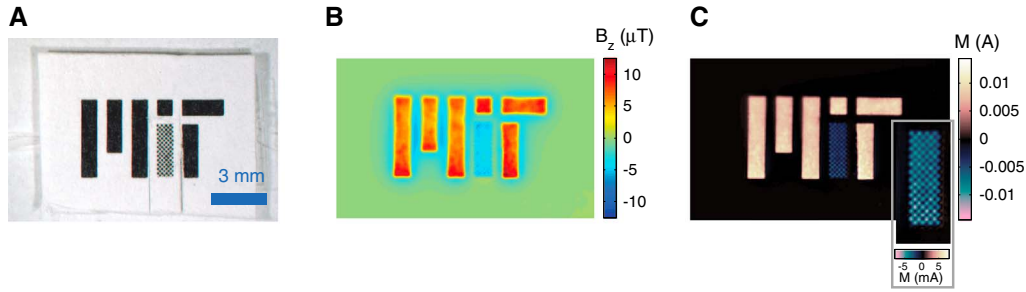
Figure 11. Inversion of experimental magnetic field data for a sample with unidimensional magnetization distribution. (a) Optical picture of synthetic consisting of MIT's logo printed on a small piece of paper. An IRM (400 mT peak field) was imparted in the $+z$ direction with the exception of the lower part of the letter "I," which was cut out, magnetized in the antipodal direction $-z$ using the same peak field, and then taped back together. (b) Z component field map of the sample shown in Figure 11A measured with our SQUID microscope. The map was measured on a 256×414 rectangular grid of positions $180\,\mu m$ above the sample with a step size of $35\,\mu m$. (c) Inversion of the field map shown in Figure 11B obtained with split regularization together with prewindowing. Observe the much sharper and well-defined edges of the individual rectangles forming the logo, indicating an improvement in spatial resolution compared to the original field map. Inset: detail of the main part of the letter "I" showing that the hatched pattern in the recovered magnetization matches the one seen in the optical picture. Because the Fourier technique does not strictly enforce positivity, high-quality recovery of such an antipodal magnetization distribution is possible. Color scale in Figure 11C inset is lightly saturated to help visualize details of the magnetization.

magnitude of the two-dimensional Fourier transform (Figure 10E) confirms that the frequency spectrum is essentially comprised of low spatial frequencies only. [Notice that the limits of the frequency axes correspond to the maximal spatial frequencies that can be represented in the discrete domain for a step size of 75 μm (i.e., $\pm\pi/\Delta$, where Δ is the mapping step size). Decreasing the regularization too much led to an inversion with artifacts around the two left vertices of the five-pointed star (Figure 10F). In this case, the spectrum (Figure 10G) contains an excess of high-frequency content that extends to the maximal spatial frequencies. This creates a cropping of the spectrum that leads to artifacts in the solution. Further adjustment of the regularization parameters yielded a solution with good balance between spatial resolution and incidence of artifacts (Figure 10H). The associated frequency spectrum (Figure 10I) displays considerable high-frequency content but with enough distance to the maximal spatial frequencies to avoid spectral cropping effects.

[91] In general, artifacts in the spectrum of underregularized solutions associated with excessive amplification of noise and spectral undulations may also be visible in those plots, depending on instrument and environmental noise levels and the size of mapping areas. If this occurs, increased regularization must be introduced to prevent peaking in the spectral content as well as to ensure spectral decay near the maximal frequencies. This means decreasing the spatial resolution, which is expected because of spectral deterioration due to increased noise levels and/or finite mapping area effects.

3.2.2. Unidimensional Case

[92] As a follow-up to the last example in section 3.1, we then inverted a unidimensional magnetization comprised of the MIT logo in which the main part of the letter "I" was magnetized into the plane ($-z$ direction) while the remainder of the logo was magnetized in the opposite direction ($+z$). In addition, the letter "I" (excluding the dot) consisted of a

dithered pattern instead of a solid one. In this case, we can assess the inversion of unidimensional distributions without the additional presence of superimposed silent sources. Figure 11A shows a photograph of the sample, and Figure 11B shows the map of the z component of the field measured 180 μm above the sample. We calculated an inversion using split regularization and postwindowing (Hann—see Appendix A) (Figure 11C). The increase in spatial resolution relative to the field map and absence of artifacts is clear: in the recovered magnetization, the edges of the rectangles are much sharper and straighter, and the dithering pattern matches perfectly the one seen in the optical picture.

3.2.3. Bidirectional Case

[93] We concluded our tests with synthetic samples by inverting a distribution that is magnetized in two different directions that are not antipodal (bidirectional magnetization). Clearly, our unidirectional magnetization model is inadequate to reproduce such a distribution. However, Appendix equation (B10) shows that if one of the directions used in the inversion is correct, the recovered distribution is always comprised of the sum of a correct inverted component and an incorrect one. This means that if there is enough spatial separation between the regions containing the two components, we can still individually reconstruct at least part of the magnetization accurately. Such a behavior is quite contrasting to techniques in the spatial domain that rely on matching of field maps, in which case the whole solution is affected in an attempt to minimize the residual. We also use this example to demonstrate what happens when a unidirectional magnetization is reconstructed using an incorrect direction.

[94] Figure 12A shows a picture of the synthetic sample comprised of the INRIA logo. The paper was cut along the small gap separating the letters "N" and "R," and each piece was magnetized separately. The letters "IN" were magnetized in the horizontal plane ($\theta = 93°$, $\varphi = 191°$), whereas the
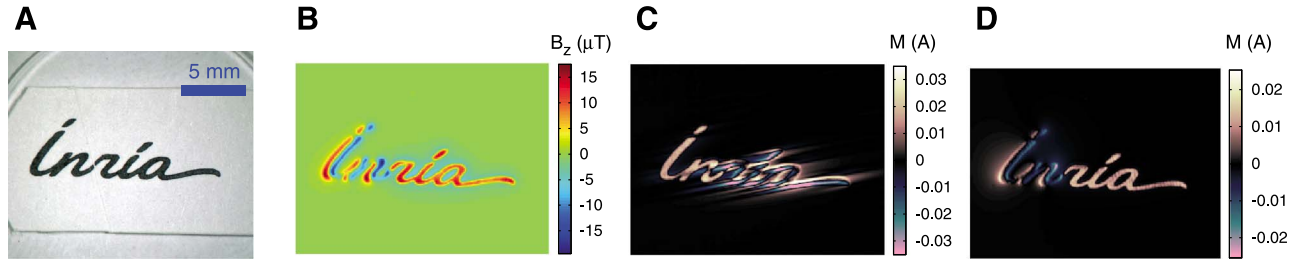
A **B** **C** **D**

Figure 12. Inversion of magnetic field data for a synthetic sample consisting of INRIA's logo printed on a small piece of paper. A bidirectional IRM (peak field of 400 mT) was imparted by cutting the paper along the existing gap between the letters "N" and "R." The letters "IN" were magnetized in the sample plane in the direction ($\theta = 93°$, $\varphi = 191°$), whereas the letters "RIA" were magnetized mostly out of the plane in the direction ($\theta = 18°$, $\varphi = 280°$). The logo was subsequently taped back together on a quartz disc. (a) Optical picture of the synthetic sample. (b) Z component field map of the sample shown in Figure 12A measured with our SQUID microscope. The map was measured on a 300×400 rectangular grid of positions $200 \, \mu m$ above the sample with a step size of $50 \, \mu m$. (c) Inversion of the field map shown in Figure 12B obtained with split regularization assuming unidimensional magnetization oriented in the direction ($\theta = 93°$, $\varphi = 191°$). Notice that the letters "IN" are well reconstructed, whereas the "RIA" letters exhibit extended artifacts due to the incorrect recovery direction for that segment of the sample. Some of these artifacts actually extend over the "N" letter. (d) Inversion of the field map shown in Figure 12B obtained with split regularization along the direction ($\theta = 18°$, $\varphi = 280°$). Notice that, in this case, the letters "RIA" are the ones well reconstructed, whereas the "IN" letters exhibit artifacts around them due to the incorrect recovery direction for that segment of the sample.

remainder of the logo was magnetized in the off-plane direction ($\theta = 18°$, $\varphi = 280°$). The two pieces of paper were then taped back together and mounted on a quartz disc. Figure 12B displays the map of the z component of the magnetic field measured $200 \, \mu m$ above the sample. Notice that the bidirectional character of the magnetization can be directly observed in the field map. Figure 12C shows the inversion calculated along the first direction (in-plane) using split regularization. A careful inspection of the solution reveals that, in fact, the letters "IN" are well reconstructed but that there is superimposed streaking originating from the second component reconstructed with the incorrect direction. Specifically, the letter "I" is mostly free of artifacts, whereas the adjacent streaking extends partly over the letter "N." An inversion calculated with the same method for the second direction (off-plane) is shown in Figure 12D. Here, the situation is reversed: the letters "RIA" are well reconstructed, while the letters "IN" exhibit streaking. Because the artifacts are much more concentrated in space in the latter case, the second component of the bidirectional magnetization is almost free of superimposed artifacts.

3.3. Geological Samples

[95] Having tested the technique and characterized its performance under various controlled conditions, we proceeded to invert magnetic data measured from $30 \, \mu m$ thin sections of actual geological samples. We began by revisiting the NRM and sIRM inversions for the sample of Hawaiian basalt first presented in Weiss *et al.* [*Weiss et al.*, 2007a, 2007b]. This sample not only provides an excellent opportunity to test the technique on a well-studied specimen, but also allows the comparison with results previously obtained using spatial-domain inversion techniques. We follow this demonstration of the technique with an inversion to identify the spatial distribution of high-coercivity grains in a $30 \, \mu m$ thin section of the eucrite meteorite ALHA81001 (a basaltic achondrite

thought to be from asteroid Vesta) that highlights the power of scanning magnetic microscopy [*Fu et al.*, 2012].

[96] Figure 13A shows a photograph of the $30 \, \mu m$ thin section of tholeiitic basalt taken from a Hawaiian Scientific Drilling Project 2 core (see [*Weiss et al.*, 2007a] for a complete description of the sample). The z component of the magnetic field of the natural remanent magnetization was measured $190 \, \mu m$ above the sample and then bilinearly interpolated by a factor of 2 (Figure 13B) to extend the spatial frequency range where the inversion is calculated. After completing the demagnetization sequence of NRM, the sample was given a sIRM, which was then mapped at the same height as the NRM. The map of the sIRM field was also interpolated by a factor of 2 (Figure 13C). We performed the inversion of the NRM field map using Wiener deconvolution together with postwindowing (Hann). The recovered NRM magnetization distribution (Figure 13E) displays a strong correlation with textural features observed in the optical image shown in Figure 13A. The recovered NRM direction was ($\theta = 40°$, $\varphi = 130°$), and the net moment calculated by integrating the reconstructed magnetization was $6.8 \times 10^{-8} \, Am^2$. The recovered sIRM magnetization distribution (Figure 13F) also exhibits a strong correlation with features observed in the optical image shown in Figure 13A. The recovered sIRM direction was ($\theta = 0°$), and the net moment calculated by integrating the reconstructed sIRM magnetization was $2.4 \times 10^{-6} \, Am^2$.

[97] Comparison with previous results obtained with a technique in the spatial domain [*Weiss et al.*, 2007a] reveals many similarities and also some noteworthy discrepancies, apart from the significant improvement in inversion speed (see Table 2 and Figure 13D). For the NRM inversion, while the overall appearance of the recovered magnetizations is similar, the Fourier reconstruction not only displays fewer artifacts but also better compromise between spatial resolution and noise magnification. Specifically, while a few features
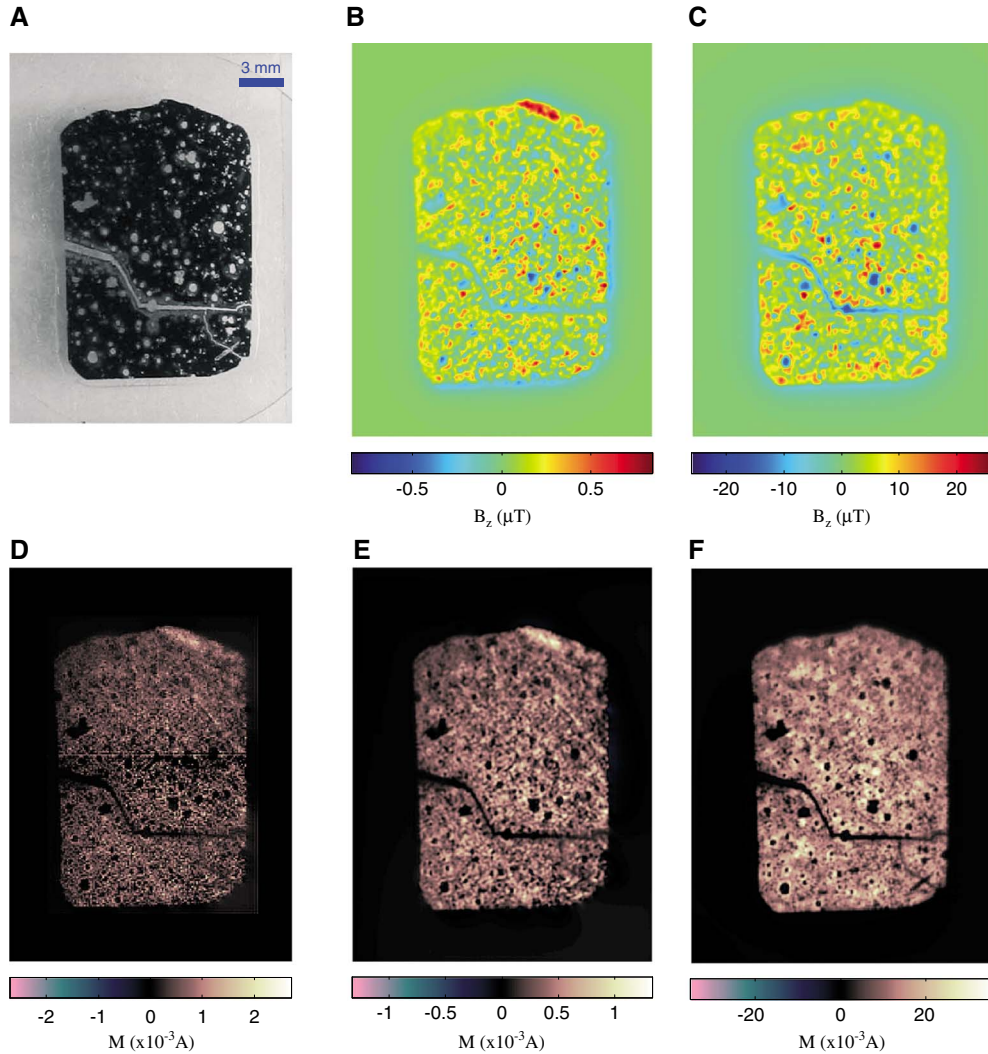
Figure 13. Inversion of magnetic field data for a 30 μm thin section of Hawaiian basalt previously analyzed in *Weiss et al.* [2007b, 2007c] using spatial-domain techniques. (a) Reflected-light picture of the thin section. (b) *Z* component magnetic field map of the natural remanent magnetization of the thin section measured with our SQUID microscope on a 250×200 rectangular grid of positions 190 μm above the sample with a step size of 100 μm. The original NRM field map was subsequently bilinearly interpolated to produce a 500×400 field map with a step size of 50 μm. (c) *Z* component magnetic field map of the saturation IRM of the thin section measured with our SQUID microscope on a 250×200 rectangular grid of positions 190 μm above the sample with a step size of 100 μm. The original sIRM field map was subsequently bilinearly interpolated to produce a 500×400 field map with a step size of 50 μm. (d) Inversion of the NRM field map shown in Figure 13B obtained with the spatial-domain technique described in *Weiss et al.* [2007a]. Because source elements were distributed in a region smaller than the field map, the recovered magnetization shown in this figure was padded with zeros so as to yield the same size as the Fourier model. Notice the artifacts located around the edges of the spatial-domain model, as well as in the middle of the magnetization distribution. The latter are due to splitting the inversion into two separate inverse problems for the top and bottom parts of the field map, respectively, to lessen memory requirements. (e) Inversion of the NRM field map shown in Figure 13B obtained with Wiener deconvolution and postwindowing. (f) Inversion of the sIRM field map shown in Figure 13C obtained with Wiener deconvolution and postwindowing.

in the spatial-domain inversion might appear sharper, this comes at the expense of accuracy—indicated by moderate peaking in the solution and larger errors in the estimated net moments—very much like what is observed in the example shown in Figure 10F. The Fourier solution also does not exhibit weak artifacts located near the sample's

edges like the spatial-domain NRM inversion does. Regarding the sIRM inversion, both inversion techniques yield solutions that are free of artifacts around the edges of the sample. However, unlike the spatial-domain inversion, the Fourier solution does not suffer from artifacts associated with segmentation of the field map to solve smaller

Table 2. Comparison of Several Magnetization Parameters Obtained With the Fourier Inversion Technique, Spatial-Domain Inversion Technique, and Bulk Moment Measurements[a]

	Spatial Domain	Fourier Domain	Rock Magnetometer
Net Moment - NRM	9.0×10^{-8} Am^2	6.8×10^{-8} Am^2	6.4×10^{-8} Am^2
Polar angle θ - NRM	47°	40°	45° ± 3°
Azimuthal angle φ - NRM	122°	130°	120° ± 3°
Peak magnetization - NRM	83 A/m	44 A/m	−
Net Moment - sIRM	1.6×10^{-6} Am^2	2.5×10^{-6} Am^2	2.2×10^{-6} Am^2
Polar angle θ - sIRM	0°	0°	0° ± 1°
Azimuthal angle φ - sIRM	0°	0°	2° ± 1°
Peak magnetization - sIRM	1700 A/m	1180 A/m	−

[a]The spatial-domain results were obtained by *Weiss et al.* [2007a].

spatial-domain inverse problems in order to reduce memory and processing requirements. Perhaps the most striking difference between inversions obtained with the two methods lies in peak magnetization strengths. When adjusted for A/m units by taking into account sample thickness, the NRM Fourier inversion has a peak strength of 44 A/m as opposed to the 83 A/m obtained in the spatial-domain inversion. The sIRM also exhibits a significant discrepancy in peak strength, with the Fourier inversion reaching 1180 A/m while the spatial-domain inversion peaks at 1700 A/m.

[98] Table 2 presents a comparison of different estimated magnetization parameters using the two techniques. In general, the Fourier inversions yielded estimated magnetization parameters much closer to the bulk measurements made
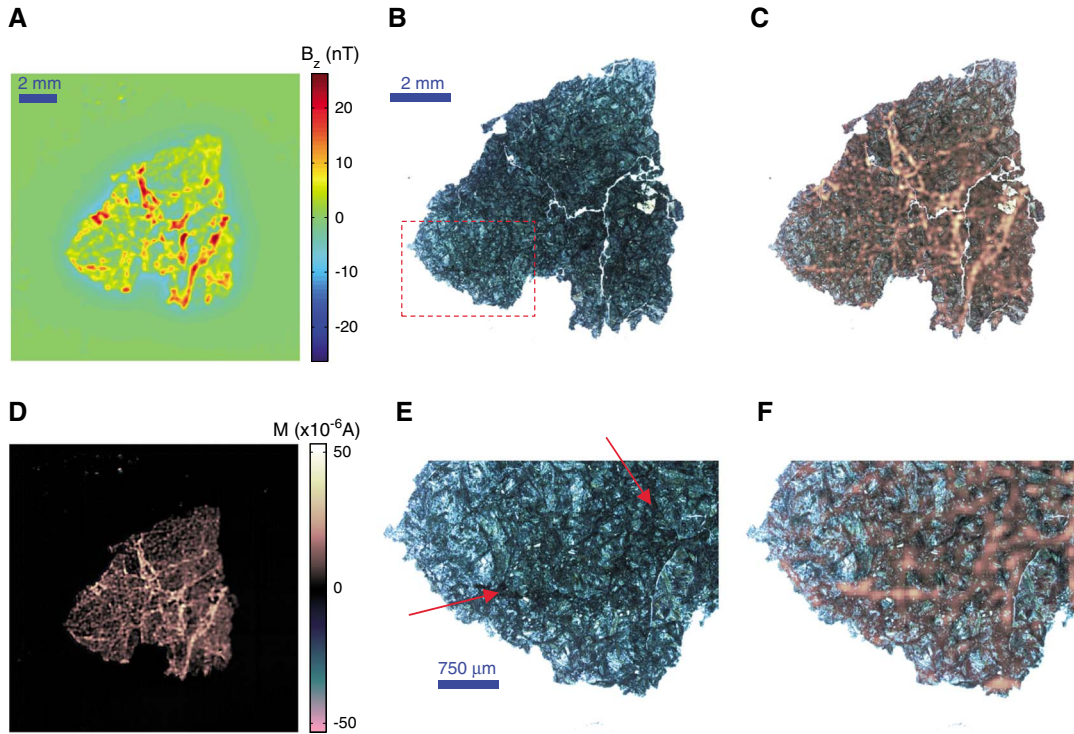

Figure 14. Inversion of magnetic field data for a 30 µm thin section of the HED meteorite ALHA81001. Following a sequence of alternating field (AF) demagnetization steps of the NRM, a strong-field IRM was imparted along the +z direction (peak field 280 mT). A 50 mT AF demagnetization step was subsequently applied prior to mapping to remove contributions from low and medium coercivity grains. (a) *Z* component magnetic field map of the thin section measured with our SQUID microscope on a 300×300 square grid of positions 190 µm above the sample with a step size of 50 µm. The original field map was subsequently bilinearly interpolated to produce a 600×600 field map with a step size of 25 µm. (b) Crossed-polars transmitted-light photograph of the thin section. Red dashed rectangle delimits the region corresponding to the magnified views shown in Figures 14E and 14F. (c) Transmitted-light photograph shown in Figure 14B with the retrieved magnetization (shown in Figure 14D) superimposed. Notice the strong correlation between source distribution and textural features. (d) Inversion of the field map data shown in Figure 14A obtained with split regularization. (e) Detailed view of the bottom left section of the photograph shown in Figure 14B. Red arrows indicate dark regions containing fine-grain assemblages of plagioclase and silica glass together with accessory ilmenite and troilite. (f) Detailed view of the bottom left section of the image shown in Figure 14C.

with a superconducting rock magnetometer. The only exception is the NRM direction; for this quantity, the spatial-domain technique recovered magnetization angles closer to the ones obtained for the bulk moment. Interestingly, this is the case where the spatial-domain solution exhibits artifacts around the edges of the magnetization, which suggests that at least one of the directional parameters was retrieved with less accuracy by that technique when searching for the best direction. Indeed, we interpret the direction obtained via Fourier method as more accurate because (i) the presence of artifacts in solutions computed for directions closer to the measured net moment direction suggests a slight streaking effect taking place due to an error in the magnetization direction (cf. section 3.2.3 and Appendix B.4), and (ii) such a small deviation in direction from the measured net moment (~8° total angular deviation) could easily be attributed to minor registration errors—particularly in declination—between the commercial magnetometer and the SQUID microscope, which were located in different laboratories at the time of those measurements, and to weak background sources (e.g., sample mounts and holders) slightly skewing the measured net moment.

[99] Regarding the discrepancy in peak values between inversions using the two methods, stronger peaks would be expected in underregularized solutions. In fact, one of the drawbacks of the iterative unidirectional inversion method in the spatial domain presented in *Weiss et al.* [2007a] is the lack of explicit regularization parameters. In that case, regularization can only be indirectly adjusted by changing the criteria for stopping the iterations, which are difficult to optimize given the much slower speed of that method. Incorporating Tikhonov regularization into the matrix formulation in our spatial-domain method could possibly ameliorate this issue, as it allows for greater control over the trade-off between spatial resolution and noise magnification, leading to solutions with fewer artifacts and better overall accuracy. The most straightforward approach consists of increasing the number of rows in the matrix to directly incorporate the constraints associated with Tikhonov regularization. The disadvantages of this approach include (i) an increase in memory requirements, which are already substantial in that method; (ii) slower speeds due to handling of larger matrices; and (iii) uncontrolled interaction between the Tikhonov regularization and the nonnegativity constraint. Whereas using algorithms specifically developed to combine both regularization and nonnegativity constraints may partly overcome such difficulties [e.g., *de Villiers et al.*, 1999; *Rojas and Steihaug*, 2002], finding the optimal regularization parameters by standard techniques (e.g., the L-curve method) would still be very time consuming and would only be advantageous in situations where spatial-domain methods offer a clear advantage over Fourier methods.

[100] Last, we applied our technique to identify the distribution of high-coercivity grains in the eucrite ALHA81001. To this end, we imparted a strong-field IRM to the thin section and subsequently applied an alternating-field demagnetization step of 50 mT to remove the contribution of low- and medium-coercivity grains. The *z* component of the magnetic field was mapped at a liftoff distance of 190 μm (Figure 14A), and we performed an inversion of the field map using split regularization (Figure 14D). Figure 14B shows a crossed-polars transmitted-light photograph of the thin section revealing detailed textural patterns. On this image, we superimposed the reconstructed distribution to show the strong correlation between high-coercivity grains and textural features. In particular, fine-grained assemblages of plagioclase and silica glass together with accessory ilmenite and troilite (dark regions in Figures 14B) consistently correlate with areas of strong magnetization, whereas larger pyroxene lathes (seen as brighter regions in Figure 14B) are much less magnetized. To better visualize those distinct regions, we show in Figures 14E and 14F detailed views of the bottom left sections of Figures 14B and 14C, respectively. Red arrows indicate examples of regions containing such fine-grained assemblages that clearly correlate with places where the magnetization distribution is strong.

[101] This magnetization distribution is consistent with our expectation that the primary ferromagnetic minerals in ALHA81001, sulfides and metal, should be concentrated in the late stage melt [*Fu et al.*, 2012]. If the ferromagnetic minerals in ALHA81001 had instead been mostly weathering products produced on Earth during the meteorite's residence in Antarctica, we might expect them to be more homogenously distributed throughout the meteorite. In that case, a general brown stain would be visible at scales >1 mm, as new ferromagnetic minerals like goethite, magnetite and hematite would fill cracks and holes that permeate the surrounding silicate phases [*Al-Kathiri et al.*, 2005; *Weiss et al.*, 2010]. Therefore, SQUID microscopy provides important evidence supporting the possibility that this meteorite could retain a record of an ancient magnetic field on its parent body. We show elsewhere [*Fu et al.*, 2012] that such assemblages in ALHA81001 in fact have retained a record of the crustal magnetic field in the asteroid 4 Vesta at about 3.69 billion years ago, which was likely produced by an earlier dynamo. This application clearly demonstrates how scanning magnetic microscopy can provide invaluable information that is complementary to traditional paleo- and rock magnetic techniques on bulk samples.

4. Conclusion

[102] We used simulated magnetizations, synthetic samples, and actual thin sections of representative terrestrial and extraterrestrial rocks to illustrate the performance of our technique. We have demonstrated that high-quality inversions can be obtained even when recovering discontinuous distributions and magnetizations corrupted by additive noise. We summarize below the key aspects of our technique:

[103] 1. Inversion of unidirectional magnetizations with compact support is unique, since all unidirectional silent sources have infinite extent.

[104] 2. Recovering fully in-plane unidirectional magnetizations often requires additional regularization to filter out ridge-like silent sources, since the formulation of the inverse problem in the Fourier domain implicitly assumes that magnetization distributions may have infinite extent.

[105] 3. Wiener deconvolution implements a trade-off between high-pass filtering (inverse filtering) and low-pass filtering (noise smoothing) based on the SNR at each spatial frequency.

[106] 4. Split regularization decouples regularization of the downward continuation operator from the regularization for the inverse directional derivative operator.

[107] 5. In both approaches, regularization parameters are adjusted heuristically to provide a compromise between high spatial resolution and occurrence of visible artifacts in the solution.

[108] 6. Accuracy in the inversion is limited by: (i) levels of noise contamination in the magnetic field data; (ii) size of the mapping area; and (iii) ratio between scanning step size and liftoff (i.e., maximum spatial frequency for which the deconvolution is computed).

[109] 7. Additional signal processing may be necessary to improve nonnegativity and to curb artifacts in the solution caused by finite mapping areas.

[110] 8. When not known a priori, the magnetization direction can be estimated by solving the inverse problem repeatedly for different assumed magnetization directions while minimizing the incidence of source elements with negative intensity.

[111] The novel contributions of this work include:

[112] 1. Efficient regularization methods combining various signal processing techniques to achieve fast and accurate inversions with superior spatial resolution while avoiding the occurrence of artifacts in the solutions.

[113] 2. Original regularization method of the downward continuation operator by the use of a special scaling function (split regularization).

[114] 3. Characterization of all magnetically silent sources affecting the inversion of unidirectional planar magnetization distributions.

[115] 4. Demonstration that the out-of-plane magnetic field component provides the best data for inversions in scanning magnetic microscopy.

[116] 5. Comprehensive analysis of numerous factors negatively impacting inversion quality—such as mapping area size and discretization of the inverse problem—and description of techniques to mitigate their effects on the solution.

[117] 6. Quantification of the recovery error and its spatial distribution under various conditions for the inverse problem in scanning magnetic microscopy.

[118] 7. High-resolution images of the spatial distribution of high coercivity grains in a thin section of the meteorite ALHA81001 and correlation with petrographic data.

Appendix A: Discretization and Mapping Area Effects

[119] Discretization of the inverse problem plays a key role in the quality of the magnetization estimates. Although amplitude discretization issues (e.g., quantization noise) can be made virtually negligible by today's ubiquitous 16 bit digital acquisition cards with amplitude range selection, several other factors may contribute to the degradation of the solution. Here, we will discuss strategies to mitigate two key problems that result from practical constraints on instrumentation: (i) the spatial resolution of field measurements is limited and (ii) the field is only measured on a small fraction of the infinite horizontal plane. The problem is that equations (2)–(4) implicitly assume knowledge of a component of the magnetic field with infinite spatial resolution over the whole plane $z = h$. As a result, position discretization and map cropping introduce a series of artifacts and limitations that may significantly impact the reconstruction of magnetization distributions.

[120] Sampling in space of magnetic fields for constructing maps is perhaps the most evident issue. Constant step sizes are often used in the measurement of magnetic field maps, which corresponds to using fixed spatial sampling frequencies. Step sizes in the x and y directions should preferably be identical, so as to avoid directional discrepancies in spatial resolution. (In this article, we assume gridding/resampling algorithms may always be utilized to achieve consistent sampling should instrumentation particularities preclude the use of identical step sizes in both horizontal directions.) Here, the Nyquist sampling theorem plays a key role, but in an oblique way: whereas one field component (often the vertical component) is usually the quantity mapped, for inversion purposes, the step size should be fine enough to correctly sample the underlying *magnetization distribution*—what we wish to recover—which is essentially unknown. Since field maps are in effect low-pass filtered versions of their corresponding magnetization distributions, owing to the exponential decay nature of the upward continuation operator, proper sampling of the field does not necessarily guarantee adequate sampling of the magnetization. Moreover, geological samples have finite dimensions, and, consequently, the Fourier transform of the magnetization distribution is not strictly band limited. This means a certain degree of aliasing will always occur when discretizing the magnetization. Nevertheless, given that physical magnetization distributions do not usually contain sharp boundaries, the magnitude of the transform decays fairly rapidly with frequency, and the spectrum may be considered band limited for practical purposes. If the discretized field map is free of aliasing, we can safely upsample it by means of interpolation/filtering algorithms so as to achieve the step size required for adequate sampling of the underlying magnetization. However, owing to noise contamination and other imperfections that might be present in experimental maps, it is sometimes beneficial to work with smaller step sizes from the start by measuring an oversampled field map.

[121] Sampling of the magnetization in space corresponds to replacing the continuous distribution with an array of magnetic dipoles spaced by a distance equal to the step size. Because sampling is mathematically equivalent to multiplying a continuous function by an impulse train (Dirac comb), integral equation (1) is replaced with a double sum of magnetic dipoles. This means that we are not approximating a continuous distribution by a piecewise constant one (zero-order hold) comprised of small uniformly magnetized rectangles. Instead, we are replacing it with a distribution of point sources, which is a coarser approximation, particularly for liftoffs that are less than several times the dimensions of the discretization element. While using smaller step sizes decreases the dipole approximation error, it leads concomitantly to the magnification of artifacts in the spectrum. Consequently, there is a trade-off between accuracy in the model and undulations in the solution. This point will be made clearer in the discussion that follows.

[122] The other main factor that leads to degradation of recovered magnetizations is finite mapping areas. In this case, the problem stems from convolutions of the source distribution with the Green's functions in equation (5). Even if a magnetization distribution has finite dimensions (compact support), its associated magnetic field will

extend to infinity owing to those convolution operations. As a result, we will only have access to a fraction of the real field map in view of the impracticality of mapping very large areas. This problem is perhaps best understood in the continuous domain, separate from position discretization. A cropped field map may be regarded as the actual infinitely supported field map multiplied by a characteristic function (rectangular window function) defining the mapping area:

$$\widetilde{B}_z(x,y) = B_z(x,y)X(x,y), \qquad (A1)$$

where the characteristic function $X(x,y) = 1$ for (x,y) lying inside the mapping area and zero otherwise. In the Fourier domain, this product becomes a two-dimensional convolution

$$\widetilde{b}_z(\kappa_x, \kappa_y) = b_z(\kappa_x, \kappa_y) * \chi(\kappa_x, \kappa_y), \qquad (A2)$$

where

$$\chi(\kappa_x, \kappa_y) = L_x L_y \operatorname{sinc}(\kappa_x L_x/2\pi) \operatorname{sinc}(\kappa_y L_y/2\pi), \qquad (A3)$$

for a rectangular mapping area extending from $(-L_x/2, -L_y/2)$ to $(L_x/2, L_y/2)$, and $\operatorname{sinc}(u) = \sin(\pi u)/\pi u$. (This function is illustrated in Fig. S5)

[123] The convolution of the spatial frequency spectrum of the true field map with sinc functions produces two main effects: (i) broadens the spectrum, and (ii) creates undulations in the spectrum. Effect (i) forces the spectrum of a cropped field map to extend to infinity, whereas effect (ii) is caused by the oscillations associated with the product of sine functions in (A3). Even if mapping areas were not rectangular, oscillations in the spectrum would still be present [e.g., the product of Bessel functions (jinc functions) for circular mapping areas]. These oscillations are further amplified by the downward continuation operator at high frequencies, as well as by the inverse directional derivative operator near the regions of the spatial frequency plane listed in Table 1.

[124] It is important to realize that such an excessive amplification takes place even for ideal noiseless maps, and that regularization has to be adjusted to cope with this effect. The manifestation of (ii) on the inverse solution usually consists of high-frequency ripples that may easily dominate the solution. Manually increasing the regularization amount tames the ripples at the expense of decreasing spatial resolution. One useful trick to minimize this type of artifact comprises premultiplying the field map by a two-dimensional window function that is not the rectangular one (boxcar) and possesses better spectral characteristics, such as reduced sidelobes [*Marple*, 1987]. While the rectangular window function has the narrowest main lobe of all windows, its sidelobes are noticeably pronounced, which leads to the aforementioned undulations in the spectrum. On the other hand, windows that begin to taper off too quickly, like the Gaussian window, have a tendency to produce solutions that exhibit a similarly tapered appearance, thus negatively impacting accuracy away from the central region of the magnetization distribution.

[125] We have found that the Tukey window exhibited superior performance compared to these other choices, in part due to its tuning capability by means of a normalized parameter, α. This allows for a good compromise between accuracy away from the center ($\alpha = 0$, rectangular window) and undulation reduction ($\alpha = 1$, Hann window). We designate this operation "prewindowing," as it corresponds to the application of a window in the spatial domain prior to calculating the inversion. Clearly, increasing the mapping area is always beneficial, as it compresses the sinc functions in (A3) and narrows the mainlobe of the window, with similar effects in other window functions. Therefore, it is always a good practice to map the field well past the sample's boundaries whenever feasible.

[126] It is also important to highlight the connection between step sizes used in the field maps and ripples in the inversions. The step size determines the maximum spatial frequency calculated by the discrete Fourier transform (DFT) and, therefore, the region where equation (33) is computed. In essence, the smaller the step size, the larger the region in the spatial frequency plane where the deconvolution is computed (i.e., higher spatial resolution) and the more amplification of both noise and spectral undulations takes place. In particular, the ratio between step size and liftoff is a critical parameter that determines the trade-off between noise magnification and spatial resolution.

Appendix B: Experimental Errors and Accuracy Issues

[127] In addition to discretization, other sources of errors and inaccuracies play a significant role in the overall quality of the solutions to the inverse problem obtained in practice. We discuss below the most relevant ones.

B1. DFT, Spectral Sampling, and Linear Convolutions

[128] The DFT (in particular, its fast-algorithm implementation—FFT) is often utilized to approximate continuous Fourier transforms in computers. A key point is the proper utilization of zero padding to ensure that linear convolutions are calculated instead of circular convolutions when multiplying DFTs. For a discretized map with $N_1 \times N_2$ points, zero padding must be introduced so as to expand the map to, at least, $(2N_1 - 1) \times (2N_2 - 1)$ points (assuming the inverse filter is discretized such that it also has $N_1 \times N_2$ points). Additional zero padding may be beneficial to improve accuracy by virtue of finer sampling of the continuous spectrum, particularly for small maps (less than 100×100 points).

[129] A second issue is that, despite dealing with finitely supported sequences, the DFT implicitly operates on infinitely supported sequences. This stems from the periodic extension of sequences utilized in the definition of the discrete transform. As a consequence, inversions may exhibit ridge-like artifacts associated with infinite-support magnetizations, such as the ones listed in Table 1.

[130] Last, care should be taken when computing the regularized inverse filter [e.g., equation (36)] so as to ensure it is sampled in frequency the same way the specific DFT/FFT algorithm used in the implementation of the inversion samples the continuous spectrum.

B2. Recovering the Uniform Magnetization Component

[131] As mentioned in section 2, the uniform component (mean value) of the magnetization distribution cannot be recovered directly from field maps. This is a direct consequence of the condition $\kappa = 0$ for breakdown of equations (23)–(25). However, if the field maps utilized in the inversion extend

past the sample's boundaries, it is still possible to recover this number accurately. Given that each source element in the Fourier formulation shares the same horizontal coordinates with a corresponding point in the field map, the source model is automatically extended past the sample as well. Therefore, because the magnetization is zero outside the sample's boundaries by definition, the uniform component is equal to the constant that should be added to the source model so as to bring the magnetization to zero outside of the sample region. Clearly, this constant automatically adjusts the magnetization within the sample, thus yielding the correct values.

B3. Nonnegativity and Ringing

[132] Residual ringing in the solution that might still be present after the prewindowing processing may often be tamed—and nonnegativity improved—by multiplying the spectrum of the solution by a suitable two-dimensional window function, before taking the inverse Fourier transform. This "postwindowing" procedure is equivalent to low-pass filtering the solution with a smooth spatial frequency response given by the window function. Notice that this windowing operation is performed in the frequency domain, whereas the prewindowing operation mentioned in Appendix A to decrease undulations in the spectrum is carried out in the spatial domain. Consequently, their effects on the solution are quite different. The main advantage of utilizing window functions instead of conventional digital filters is the better control over ringing, considering that sharp selectivity is not required nor desired. Postwindowing gradually tapers off the spectrum so as to make it zero at the edges of the region in the spatial frequency plane where the DFT is computed. It is advantageous to parameterize the window function in order to stretch or shrink its spatial frequency response, thus controlling the passband of the filter. Postwindowing can be regarded as the two-dimensional convolution in the spatial domain between the inverse solution and the inverse Fourier transform of the window function. Typically, the Hann window yields a good compromise between spatial resolution and ringing reduction.

B4. Imprecision in Sensor-to-Sample Distance and Magnetization Direction

[133] In this section, we analyze the effects on the solution of using incorrect liftoffs and magnetization directions. Uncertainties in the estimation of these two parameters due to experimental error or lack of a priori information may negatively impact the quality of the inversions. Recognizing the nature of artifacts that might eventually be present in the solution to the inverse problem is key to distinguishing between the sources of inaccuracy.

[134] Typically, the liftoff is estimated from scans of known sources of magnetic field (e.g., current-carrying thin-film wires [*Baudenbacher et al.*, 2002; *Lee et al.*, 1996]) or by using a micropositioner [*Hankard et al.*, 2009]. In the first method, the magnetic field is measured along a line perpendicular to the wire, and the experimental data are used to determine several parameters of a model, one of which is the sample-sensor separation. Clearly, this method requires a setup where samples can be swapped without changing the liftoff, so that the wire scan is representative of the distance used in the mapping of actual samples. In the second method—which is only suitable for sensors operating at room temperature—a micropositioner

controls the separation by displacing vertically either the sensor or the sample. Here, the sensor first touches the surface of the specimen, establishing a reference point, which corresponds to the smallest possible separation. Next, the liftoff is adjusted and measured by means of the micropositioner so as to provide a gap large enough to safely scan the sample without scratching it or damaging the sensor tip. Note that, in this case, the distance from the sample to the sensing element is not directly measured, and the location of the sensing element relative to the sensor tip must be determined by a different method. However, given that this distance is fixed for a particular sensor, it only has to be measured once and later added to the liftoff measurements.

[135] Regardless of the method chosen to measure the liftoff, there is always an error associated with these estimates. Suppose the sensor is positioned at a height h above the sample, but the inversion is calculated for an estimated liftoff of $h' = h + \Delta h$, where Δh can be positive (overestimation of the liftoff) or negative (underestimation). In this case, the calculated solution will be a filtered version of the true magnetization distribution. If $\Delta h > 0$, the spectrum experiences an exponential frequency boost. Conversely, an exponential frequency cut takes place when $\Delta h < 0$. This can be easily understood by realizing that the liftoff directly affects the downward continuation operator. Specifically, from equations (25) and (33), we have that

$$m'(\kappa_x, \kappa_y) = e^{\Delta h \kappa} m(\kappa_x, \kappa_y). \tag{B1}$$

[136] Thus, the magnitude of m' increases for $\Delta h > 0$ and decreases for $\Delta h < 0$, as $e^{\Delta h \kappa} \geq 1$ for Δh positive and $0 < e^{\Delta h \kappa} \leq 1$ for Δh negative. Overestimated liftoffs yield solutions that are excessively sharp and may contain high-frequency oscillations. Underestimated liftoffs, on the other hand, smooth the solution and decrease the spatial resolution. For small deviations from the nominal liftoff, it might be hard to perceive such effects, but they are fairly obvious for medium to large Δh or very small scanning step sizes (due to an increase in the maximum frequency for which the exponential term is calculated).

[137] The effect of using an incorrect direction to recover a unidirectional magnetization is somewhat harder to quantify. Let $\vec{K}$ denote an element in $\mathbb{C}^3$ (i.e., the vector space comprised of all vectors with three complex components) of the form $(i\kappa_x, i\kappa_y, -\kappa)$. If $\hat{u} = (\sin\theta \cos\varphi, \sin\theta \sin\varphi, \cos\theta)$ and $\hat{v} = (\sin\alpha \cos\beta, \sin\alpha \sin\beta, \cos\alpha)$—which are also elements in $\mathbb{C}^3$, as $\mathbb{R}^3 \subset \mathbb{C}^3$—represent the true magnetization direction and the estimated direction, respectively, we may rewrite equations (25) and (33) as

$$b_z(\kappa_x, \kappa_y) = -\frac{\mu_0}{2} e^{-h\kappa} \left[\vec{K} \cdot \hat{u}\right] m(\kappa_x, \kappa_y), \tag{B2}$$

$$m'(\kappa_x, \kappa_y) = -\frac{2}{\mu_0} e^{h\kappa} \left[\vec{K} \cdot \hat{v}\right]^{-1} b_z(\kappa_x, \kappa_y), \tag{B3}$$

for $\vec{K} \cdot \hat{v} \neq 0$. ($m'(\kappa_x, \kappa_y)$ is undetermined whenever $\vec{K}$ is orthogonal to $\hat{v}$, as discussed in section 2—see Table 1.
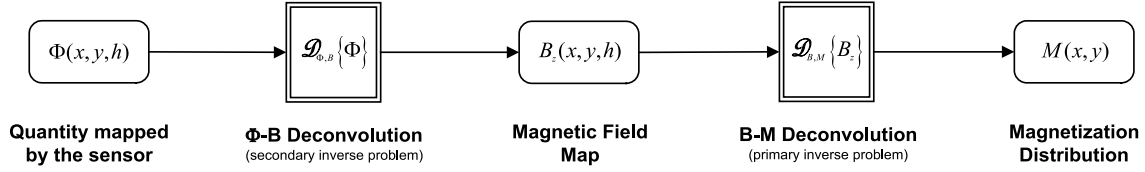
Figure B1. Diagram illustrating the composition of two inverse problems when considering sensor effective area/volume effects. A secondary inverse problem (Φ-B deconvolution) must be solved prior to the primary inverse problem for determining planar magnetization distributions from field maps (B-M deconvolution).

Notice that while $\hat{u}$ and $\hat{v}$ are fixed, $\vec{K}$ changes as κ_x and κ_y vary.) Substituting equation (B2) in equation (B3), we get

$$m'\left(\kappa_x, \kappa_y\right) = \frac{\vec{K}\cdot\hat{u}}{\vec{K}\cdot\hat{v}} m\left(\kappa_x, \kappa_y\right), \qquad (B4)$$

for $\vec{K}\cdot\hat{v} \neq 0$. Finally, using the identity $\hat{u} = \hat{v} + (\hat{u} - \hat{v})$, we have that

$$m'\left(\kappa_x, \kappa_y\right) = \left[1 + \frac{\vec{K}\cdot(\hat{u} - \hat{v})}{\vec{K}\cdot\hat{v}}\right] m\left(\kappa_x, \kappa_y\right), \qquad (B5)$$

for $\vec{K}\cdot\hat{v} \neq 0$. If $\hat{v}$ does not lie in the horizontal plane, $\vec{K}$ is never orthogonal to $\hat{v}$, and the difference between recovered and true spectra is given by

$$e\left(\kappa_x, \kappa_y\right) = m'\left(\kappa_x, \kappa_y\right) - m\left(\kappa_x, \kappa_y\right)$$
$$= \begin{cases} \dfrac{\vec{K}\cdot(\hat{u} - \hat{v})}{\vec{K}\cdot\hat{v}} m\left(\kappa_x, \kappa_y\right) & , \text{ if } \kappa_x \neq 0 \text{ or } \kappa_y \neq 0 \\ -m(0,0) & , \text{ otherwise.} \end{cases} \qquad (B6)$$

[138] The difference at $\vec{K} = \vec{0}$ (the origin of spatial frequency plane) can be made negligible, given that the uniform component may be recovered by other means (see previous discussion in Appendix B.2). However, the only way to consistently decrease $e(\kappa_x, \kappa_y)$ at all spatial frequencies (e.g., to minimize its norm) is making $\hat{v}$ as close to $\hat{u}$ as possible.

[139] In particular, it is possible to establish bounds for the recovery error. Since $\left|\vec{K}\cdot(\hat{u} - \hat{v})\right| \leq \kappa|\hat{u} - \hat{v}|$ and $\left|\vec{K}\cdot\hat{v}\right| \geq \kappa|v_z|$, we have (assuming $v_z \neq 0$)

$$\left|e\left(\kappa_x, \kappa_y\right)\right|^2 \leq \frac{|\hat{u} - \hat{v}|^2}{v_z^2} \left|m\left(\kappa_x, \kappa_y\right)\right|^2. \qquad (B7)$$

[140] Using Parseval's theorem (twice), we obtain the following upper bound for the squared error (cf. Lemma 4.2 of Baratchart *et al.* [2013]):

$$\iint_{\mathbb{R}^2} |E(x,y)|^2 dx\, dy \leq \frac{|\hat{u} - \hat{v}|^2}{v_z^2} \iint_{\mathbb{R}^2} \left|m\left(\kappa_x, \kappa_y\right)\right|^2 dx\, dy. \qquad (B8)$$

B5. Effects of Nonunidirectionality of the Actual Magnetization

[141] Equations (B2) and (B3) may also be utilized to show what happens when the real magnetization is not purely unidirectional. Let us assume the sample is magnetized in two distinct directions $\hat{u}_1$ and $\hat{u}_2$, such that $\vec{M}(x,y) = M_1(x,y)\hat{u}_1 + M_2(x,y)\hat{u}_2$. This bidirectional model may represent, for instance, overprints associated with viscous remanent magnetization, partial reheating, and IRM due to proximity to hand magnets.

[142] In this case, equation (B2) becomes

$$b_z\left(\kappa_x, \kappa_y\right) = -\frac{\mu_0}{2} e^{-h\kappa} \left\{\left[\vec{K}\cdot\hat{u}_1\right] m_1\left(\kappa_x, \kappa_y\right) \right.$$
$$\left. + \left[\vec{K}\cdot\hat{u}_2\right] m_2\left(\kappa_x, \kappa_y\right)\right\}, \qquad (B9)$$

where m_1 and m_2 are the magnetization distributions oriented along directions $\hat{u}_1$ and $\hat{u}_2$, respectively.

[143] If we invert the field map in the direction $\hat{u}_1$ [i.e., making $\hat{v} = \hat{u}_1$ in equation (B3)], we get

$$m'\left(\kappa_x, \kappa_y\right) = m_1\left(\kappa_x, \kappa_y\right) + \frac{\vec{K}\cdot\hat{u}_2}{\vec{K}\cdot\hat{u}_1} m_2\left(\kappa_x, \kappa_y\right), \qquad (B10)$$

for $\vec{K}\cdot\hat{u}_1 \neq 0$.

[144] [Notice the similarity between equations (B10) and (B5). In this case, for a magnetization off the horizontal plane, the discrepancy between the magnetization estimate and the unidirectional distribution due to the overprint is given by

$$e\left(\kappa_x, \kappa_y\right) = m'\left(\kappa_x, \kappa_y\right) - m_1\left(\kappa_x, \kappa_y\right)$$
$$= \begin{cases} \dfrac{\vec{K}\cdot\hat{u}_2}{\vec{K}\cdot\hat{u}_1} m_2\left(\kappa_x, \kappa_y\right) & , \text{ if } \kappa_x \neq 0 \text{ or } \kappa_y \neq 0 \\ -m_1(0,0) & , \text{ otherwise.} \end{cases} \qquad (B11)$$

[145] The only way to consistently decrease the error in the recovery consists of making m_2 as small as possible.

[146] It is worthwhile noticing that equation (B10) shows a key distinction between spatial-domain inversion techniques based on residual minimization and our technique: in the Fourier domain, one of the components of a multidirectional magnetization may be directly recovered provided there is enough spatial separation between the supports of the components. Even when the supports overlap, useful information may still be retrieved, as the error tends to be concentrated on and around the support of the components reconstructed using incorrect directions.

B6. Finite Sensor Area

[147] In practice, magnetic sensors do not measure the field at a point, but detect instead some form of average of the field over the sensing area (e.g., planar integrated sensing element) or sensing volume (e.g., discrete sensing element), as

Table C1. Regularization Parameters for the Inversion Examples Shown in Section 3

Figure	Reg.	Pre Wnd.	Post Wnd.	ρ or κ_0	γ or ξ	γ'	NRMSD
6c	Split	Tukey - 0.5	Hann - 0.75	0.28	0.1	1.0×10^{-21}	0.109
6e	Wiener	Tukey - 0.5	–	200	1.0×10^{-21}	–	0.099
6g	Wiener	–	–	200	1.0×10^{-21}	–	–
6h	Wiener	Tukey - 0.5	–	200	1.0×10^{-16}	–	0.161
7c	Wiener	Tukey - 0.5	–	10	2.0×10^{-20}	–	0.053
8c	Wiener	Tukey - 0.5	–	6.5	3.0×10^{-19}	–	0.217
8g	Wiener	Tukey - 0.5	–	6.5	1.0×10^{-19}	–	0.152
9d	Split	Tukey - 0.7	–	0.30	0.1	8.0×10^{-24}	0.295
9e	Split	Tukey - 0.5	–	0.26	0.9	8.0×10^{-15}	0.125
9g	Split	Tukey - 0.6	–	0.32	0.1	1.0×10^{-21}	0.358
9h	Split	Tukey - 0.5	–	0.20	0.9	5.0×10^{-10}	0.143
10d	Wiener	Tukey - 0.5	–	1.0	1.0×10^{-17}	–	–
10f	Wiener	–	–	1.0	1.0×10^{-25}	–	–
10h	Wiener	Tukey - 0.5	–	1.0	1.0×10^{-22}	–	–
11c	Split	–	Hann - 0.3	0.25	1	1.0×10^{-18}	–
12c	Split	–	–	0.25	0.9	1.0×10^{-7}	–
12d	Split	–	–	0.21	0.5	5.0×10^{-13}	–
13e	Wiener	–	Hann - 0.4	6000	5.0×10^{-20}	–	–
13f	Wiener	–	Hann - 0.4	6000	1.0×10^{-20}		–
14d	Split	–	–	0.12	1.0	1.0×10^{-18}	–
S2c	Wiener	Tukey - 0.5	–	10	1.0×10^{-20}		0.175
S3c	Wiener	Tukey - 0.5	–	6.5	1.0×10^{-19}		0.098
S4c	Wiener	Tukey - 0.5	Hann - 0.7	30	4.0×10^{-16}		0.893
S4g	Wiener	Tukey - 0.5	Hann - 0.4	305	4.0×10^{-16}		0.268

determined by the particular sensor design. We will restrict our analysis to planar sensors oriented parallel to the sample, which is a configuration widely used in scanning magnetic microscopes. However, sensor modeling may be easily extended to incorporate other orientations and configurations, such as gradiometers and discrete sensors that integrate the field over a volume [*Lima et al.*, 2002].

[148] Depending on the orientation of the device and on the liftoff relative to the size of the sensing area and to the sensor thickness, such integration effects may be neglected because the magnetic field is approximately constant within the sensing area/volume. However, in scanning magnetic microscopy, sensors are often brought in very close proximity to samples, and it is not unusual for the liftoff to be smaller than the dimensions of the sensing element, particularly for noncryogenic sensors. In this case, detailed modeling of the quantity effectively measured by the sensor is required for accurate inversions. A particularly pernicious effect is the integration along the direction normal to the sample (the z direction in our model), given that it leads to a substantial decrease in spatial resolution.

[149] To illustrate how such effects could be modeled, we assume that the sensor detects the magnetic flux threaded through a planar sensing area parallel to the sample. That is,

$$\Phi(\vec{r}) = \iint_A \vec{B}(\vec{r}) \cdot \hat{n} \, d\vec{r} = \iint_A B_z(x, y, h) \, dx dy, \quad \text{(B12)}$$

where A is the effective area of the sensor. This flux integral can be converted into a two-dimensional convolution by defining a suitable function W representing the effective area of the sensor

$$\Phi(x, y) = \int_{-\infty}^{+\infty} \int_{-\infty}^{+\infty} W(\eta, \xi) B_z(x - \eta, y - \xi) \, d\eta d\xi \quad \text{(B13)}$$

where we have again omitted the dependence on the liftoff h.

If, for example, the effective area is equivalent to a circular coil with N turns and radius a, the turns function W is given by

$$W(x, y) = \begin{cases} N, & \text{if } \sqrt{x^2 + y^2} \le a \\ 0, & \text{otherwise,} \end{cases} \quad \text{(B14)}$$

and its two-dimensional Fourier transform is

$$w(\kappa_x, \kappa_y) = 2\pi N a^2 \, \text{jinc}(a\kappa), \quad \text{(B15)}$$

where $\text{jinc}(u) = J_1(u)/u$ and J_1 is the Bessel function of the first kind and first order.

[150] Although the sensor, in practice, measures magnetic flux instead of magnetic field, we can still retrieve the field map by first solving a flux-to-field ancillary inverse problem [i.e., inverting equation (B13)] by means of pseudo-inverse filters or Wiener deconvolution. The inverted data are then fed to the inverse problem for the magnetization given by equation (1), as illustrated in Figure B1. Clearly, regularization of this flux-field deconvolution is critical, since the Fourier transform of W has an infinite number of zeros (see Fig. S6). Consequently, the deconvolution is sensitive to some of the issues previously discussed. Whereas lumping together the two inverse problems is possible in principle through adjustment the Green's function, a great degree of control over the regularization could be lost, as a single set of regularization parameters must be chosen to handle all singularities. A better approach consists of separating the two inverse problems and their regularizations. Evidently, it is not necessary to compute the inverse Fourier transform at the end of the secondary inverse problem, given that it would introduce numerical error.

Appendix C: Regularization Parameters Used in the Examples

[151] We list in Table C1 the specific regularization parameters used in each of the inversions shown in section 3. We also show which regularization method was used and the corresponding NRMSD obtained (when applicable), in addition to the prewindowing and postwindowing parameters. For the Wiener deconvolution, the regularization parameters are ρ and γ [see equation (40)], whereas for the split regularization method, the parameters are κ_0 and ξ for the downward continuation operator [see equation (43)], and γ' for the inverse directional derivative operator [see equation (44)] (note that we use a prime symbol to distinguish this parameter from the one used in the Wiener deconvolution). We remark that such numbers should not be interpreted as absolute parameter values and that they may change significantly when using different samples, experimental setups, sensor technologies, step sizes, sensor-to-sample distances, and mapping areas.

References

Al-Kathiri, A., B. A. Hofmann, A. J. T. Jull, and E. Gnos (2005), Weathering of meteorites from Oman: Correlation of chemical and mineralogical weathering proxies with C-14 terrestrial ages and the influence of soil chemistry, *Meteorit. Planet. Sci.*, *40*(8), 1215–1239.

Baratchart, L., D. P. Hardin, E. A. Lima, E. B. Saff, and B. P. Weiss (2013), Characterizing kernels of operators related to thin plate magnetizations via generalizations of Hodge decompositions, *Inverse Probl.*, *29*(1), 015004.

Baudenbacher, F. J., N. T. Peters, and J. P. Wikso (2002), High resolution low-temperature superconductivity superconducting quantum interference device microscope for imaging magnetic fields of samples at room temperatures, *Rev. Sci. Instrum.*, *73*, 1247–1254.

Blakely, R. J. (1996), *Potential Theory in Gravity and Magnetic Applications*, 441 pp., Cambridge Univ. Press, New York.

Bott, M. H. P. (1967), Solution of the linear inverse problem in magnetic interpretation with application to oceanic magnetic anomalies, *Geophys. J. R. Astron. Soc.*, *13*(1-3), 313–323.

Cooley, J. W., and J. W. Tukey (1965), An algorithm for machine calculation of complex Fourier series, *Math. Comput.*, *19*(90), 297–301.

Dallas, W. J. (1985), Fourier space solution to the magnetostatic imaging problem, *Appl. Opt.*, *24*(24), 4543–4546.

Egli, R., and F. Heller (2000), High-resolution imaging using a high-T_c superconducting quantum interference device (SQUID) magnetometer, *J. Geophys. Res.*, *105*, 25,709–25,727.

Fong, L. E., J. R. Holzer, K. K. McBride, E. A. Lima, and F. Baudenbacher (2005), High resolution room-temperature sample scanning superconducting interference device microscope configurable for geological and biomagnetic applications, *Rev. Sci. Instrum.*, *76*, 053703.

Fu, R. R., B. P. Weiss, D. L. Shuster, J. Gattacceca, T. L. Grove, C. Suavet, E. A. Lima, L. Li, and A. T. Kuan (2012), An ancient core dynamo in asteroid Vesta, *Science*, *338*(6104), 238–241.

Hankard, F., J. Gattacceca, C. Fermon, M. Pannetier-Lecoeur, B. Langlais, Y. Quesnel, P. Rochette, and S. A. McEnroe (2009), Magnetic field microscopy of rock samples using a giant magnetoresistance-based scanning magnetometer, *Geochem. Geophys. Geosyst.*, *10*, Q10Y06, doi:10.1029/2009GC002750.

Huestis, S. P., and R. L. Parker (1979), Upward and downward continuation as inverse problems, *Geophys. J. R. Astron. Soc.*, *57*(1), 171–188.

Jain, A. K. (1989), *Fundamentals of Digital Image Processing*, 1st ed., 569 pp., Prentice-Hall, Englewood Cliffs, N. J.

Kletetschka, G., P. Schnabl, K. Šifnerová, Z. Tasáryová, S. Manda, and P. Pruner (2013), Magnetic scanning and interpretation of paleomagnetic data from Prague Synform's volcanics, *Stud. Geophys. Geod.*, *57*, 103–117, doi:10.1007/s11200-012-0723-4.

Kullmann, W., and W. J. Dallas (1987), Fourier imaging of electrical currents in the human brain from their magnetic fields, *IEEE Trans. Biomed. Eng.*, *34*(11), 837–842.

Lee, T. S., E. Dantsker, and J. Clarke (1996), High-transition temperature superconducting quantum interference device microscope, *Rev. Sci. Instrum.*, *67*(12), 4208–4215.

Lee, S.-Y., J. Mathews, and F. C. Wellstood (2004), Position noise in scanning superconducting quantum interference device microscopy, *Appl. Phys. Lett.*, *84*, 5001–5003.

Lim, J. S. (1990), *Two-Dimensional Signal and Image Processing*, 1st ed., Prentice-Hall, Englewood Cliffs, N. J.

Lima, E. A., and B. P. Weiss (2009), Obtaining vector magnetic field maps from single-component measurements of geological samples, *J. Geophys. Res.*, *114*, B06102, doi:10.1029/2008JB006006.

Lima, E. A., A. C. Bruno, and J. Szczupak (2002), Two-dimensional deconvolution technique to recover the original magnetic field from the flux measured by SQUID planar gradiometers, *Supercond. Sci. Technol.*, *15*(8), 1259–1267.

Mareschal, J. C. (1985), Inversion of potential field data in Fourier transform domain, *Geophysics*, *50*(4), 685–691.

Marple, S. (1987), *Digital Spectral Analysis With Applications*, 1st ed., 492 pp., Prentice Hall, Englewood Cliffs, N. J.

Mayhew, M. A. (1979), Inversion of satellite magnetic anomaly data, *J. Geophys.*, *45*(2), 119–128.

Oda, H., et al. (2011), Ultrafine-scale magnetostratigraphy of marine ferromanganese crust, *Geology*, *39*(3), 227–230.

Parker, R. L. (1973), Rapid calculattion of potential anomalies, *Geophys. J. R. Astron. Soc.*, *31*(4), 447–455.

Parker, R. L. (1977), Understanding inverse theory, *Annu. Rev. Earth Planet. Sci.*, *5*, 35–64.

Parker, R. L., and S. P. Huestis (1974), Inversion of magnetic anomalies in the presence of topography, *J. Geophys. Res.*, *79*(11), 1587–1593.

Rojas, M., and T. Steihaug (2002), An interior-point trust-region-based method for large-scale non-negative regularization, *Inverse Probl.*, *18*(5), 1291–1307.

Roth, B. J., N. G. Sepulveda, and J. P. Wikso Jr. (1989), Using a magnetometer to image a two-dimensional current distribution, *J. Appl. Phys.*, *65*, 361–372.

Saff, E. B., and A. B. J. Kuijlaars (1997), Distributing many points on a sphere, *Math. Intell.*, *19*(1), 5–11.

Schouten, H., and K. McCamy (1972), Filtering marine magnetic anomalies, *J. Geophys. Res.*, *77*(35), 7089–7099.

Talwani, M. (1965), Computation with help of a digital computer of magnetic anomalies caused by bodies of arbitrary shape, *Geophysics*, *30*(5), 797–817, doi:10.1190/1.1439654.

Tan, S., Y. P. Ma, I. M. Thomas, and J. P. Wikso (1996), Reconstruction of two-dimensional magnetization and susceptibility distributions from the magnetic field of soft magnetic materials, *IEEE Trans. Magn.*, *32*, 230–234.

Uehara, M., and N. Nakamura (2007), Scanning magnetic microscope system utilizing a magneto-impedance sensor for a nondestructive diagnostic tool of geological samples, *Rev. Sci. Instrum.*, *78*(4), 6, 043708, doi:10.1063/1.2722402.

Usui, Y., M. Uehara, and K. Okuno (2012), A rapid inversion and resolution analysis of magnetic microscope data by the subtractive optimally localized averages method, *Comput. Geosci.*, *38*(1), 145–155.

de Villiers, G. D., B. McNally, and E. R. Pike (1999), Positive solutions to linear inverse problems, *Inverse Probl.*, *15*(2), 615–635.

Volk, M., S. Whitlock, C. H. Wolff, B. V. Hall, and A. I. Sidorov (2008), Scanning magnetoresistance microscopy of atom chips, *Rev. Sci. Instrum.*, *79*(2), 023702, doi:10.1063/1.2839015.

Weiss, B. P., E. A. Lima, L. E. Fong, and F. J. Baudenbacher (2007a), Paleomagnetic analysis using SQUID microscopy, *J. Geophys. Res.*, *112*, B09105, doi:10.1029/2007JB004940.

Weiss, B. P., E. A. Lima, L. E. Fong, and F. J. Baudenbacher (2007b), Paleointensity of the Earth's magnetic field using SQUID microscopy, *Earth Planet. Sci. Lett.*, *264*, 61–71.

Weiss, B. P., J. Gattacceca, S. Stanley, P. Rochette, and U. R. Christensen (2010), Paleomagnetic records of meteorites and early planetesimal differentiation, *Space Sci. Rev.*, *152*(1-4), 341–390.